Joint modulation of coastal rainfall in Northeast Australia by local and large-scale forcings

T. L. Dao[1,2], C. L. Vincent[1,2], Y. Huang[1,2], S. C. Peatman[3,4], J. S. Soderholm[5], C. E. Birch[4], D. S. Roberts[6]

[1]School of Geography, Earth and Atmospheric Sciences and ARC Centre of Excellence for Climate Extremes, The University of Melbourne, Melbourne, Victoria, Australia.

[2]ARC Centre of Excellence for 21st Century Weather, Melbourne, Victoria, Australia.

[3] Centre for Climate Research Singapore, Meteorological Service Singapore

[4] Institute for Climate and Atmospheric Science, School of Earth and Environment, University of Leeds, United Kingdom.

[5] Science and Innovation Group, The Bureau of Meteorology, Melbourne, Victoria, Australia.

[6] Research School of Earth Sciences, The Australian National University, Canberra, Australian Capital Territory, Australia.

Corresponding author: Thi Lan Dao (thiland@student.unimelb.edu.au)

Abstract

This study investigates the impact of the interaction between large-scale and local-scale forcings in regulating rainfall patterns and their propagation over coastal areas of Northeast (NE) Australia using a convective-scale regional model run for 180 days. Over the coastal areas, spatially heterogeneous rainfall patterns are evident in both radar observations and model simulations. By classifying the characteristics of three distinct rainfall groups, we found that the rainfall propagation modulates the average rainfall patterns. Modelling results suggest that the large-scale background wind and local-scale land-sea breeze circulations are two important factors driving rainfall propagation. Offshore rainfall propagation, which is frequently observed in coastal regions in the tropics, occurs during the days with weak easterlies near surface and strong upper-and mid-level westerlies. Rainfall is triggered during the afternoon by convergence driven by the sea breeze and then propagates offshore during the nighttime with the land breeze density current and large-scale background westerlies. In contrast, onshore rainfall propagation is observed during days with strong background easterlies from the surface to upper levels. For the no propagation group, rainfall occurs during the afternoon due to the convergence of sea breezes and low-level background westerlies, and it persists over land during the nighttime with low-and mid-level easterlies. Our results also suggest that the background wind regimes associated with different phases of intraseasonal variability modulate the direction and strength of rainfall propagation, leading to different coastal rainfall patterns.

Keywords: coastal rainfall, rainfall propagation, scale interactions, high-resolution simulations

1 Introduction

The coastal region of Queensland plays an important role in Australia's agriculture, with approximately 95% of the country's sugarcane grown in this area (Smith et al., 2014). This region is also highly vulnerable to flooding as it regularly experiences heavy rainfall events (King et al., 2013; Cowan et al., 2019). Over coastal areas, the initiation, development, and propagation of precipitation are modulated by multiple processes across different spatial and temporal scales. For example, Queensland's rainfall is influenced by large-scale climate variability such as El Niño - Southern Oscillation (ENSO; McBride and Nicholls 1983; Wang and Hendon 2007; King et al., 2013), the Madden Julian Oscillation (MJO, Wheeler et al., 2009; Cowan et al., 2023; Dao et al., 2023) and the interactions between these climate modes (Ghelani et al., 2017; Cowan et al., 2023; Dao et al., 2023). Synoptic-scale processes are another factor influencing rainfall along the Queensland coast. Trade wind-associated precipitation occurs along coastal areas of northern Queensland, where predominantly southeasterly onshore flows are forced to ascend over a coastal plain with hills ranging from 100 to 500 meters in height (Connor and Bonnell, 1998, Klingaman, 2012). By analyzing 133 rain-gauge sites in the Townsville region, Lyons and Bonnel (1992) identified that flow over orography is a key factor controlling trade-wind precipitation during the wet season from October 1988 to June 1989. These studies suggest that understanding the variability in the direction and strength of low- and mid-level trade winds, as well as their relationship with large-scale climate modes, is crucial for understanding rainfall along the coast of tropical Queensland.

Over northern Queensland, coastal rainfall and its diurnal cycle are also modulated by local-scale forcings such as coastal orography (Black and Lane, 2015; Twomey and Kiem, 2021) and land-sea breezes (Short et al., 2019; Bui et al., 2023, Dao et al., 2025). Orography can affect rainfall directly by forcing local upward motion which triggers convective initiation and development, or indirectly by forcing horizontal air currents to move separately around topographic features, causing local divergence and upward motion (Klingaman, 2012). Mesoscale land-sea breeze circulations, which are driven by the differential heating between land and the adjacent ocean (Mapes et al., 2003ab; Yang and Slingo, 2001), are a major forcing of convection and rainfall diurnal cycle in the tropics (Peatman et al., 2014, 2015; Vincent and Lane, 2016, Peatman et al., 2023). Love et al. (2011) found that both onshore and offshore rainfall propagation over coastal areas of the Maritime Continent (MC) and northern Australia is strongly modulated by diurnal processes, with the diurnal rainfall amplitude accounting for approximately 50% of the mean rainfall. Using the Cyclone Global Navigation Satellite System observation to investigate the diurnal rainfall variation and its associated land-sea breeze circulation, Bui et al (2023) also found that the surface wind speed is highly correlated with the diurnal precipitation propagation over coastal tropical Australia.

In addition to the independent influences of large-scale and local-scale processes on rainfall, previous studies also examined the impact of scale interaction on precipitation over the deep tropics (Peatman et al., 2014; Rauniyar and Walsh, 2016; Lestari et al., 2022) as well as over the coastal areas of Australia (Gregory et al., 2024; Dao et al., 2023, 2025). Gregory et al. (2024) found that the MJO affects local meteorology over the Great Barrier Reef by modulating synoptic patterns against the background ENSO conditions. Dao et al. (2023) also highlighted that some coastal locations in Northeast Australia exhibit an opposite rainfall response to the typical ENSO-rainfall relationship, suggesting that ENSO's influence on rainfall is further modulated by local processes. Dao et al. (2025) examined the variation of local rainfall with the MJO using two modern S-band Doppler radars over coastal areas of north Queensland. They

found that the response of rainfall and its diurnal cycle to the MJO shows both large-scale and local-scale influences and that the locally enhanced rainfall during the suppressed MJO phases is likely co-modulated by mesoscale land sea breezes, their interaction with large-scale background wind and topography. These observational studies suggest that the impact of large-scale climate mode variability on coastal rainfall is further modulated by local-scale processes, leading to inhomogeneous rainfall patterns along the coast. However, existing observations are not sufficient to fully unpack the thermodynamic and dynamic aspects of the scale-interaction mechanisms. Therefore, high resolution modelling is needed to fully understand the physical mechanisms driving observed coastal rainfall.

High-resolution simulations have been used to investigate the impact of scale interactions between large-scale and local-scale forcings on modulating rainfall over the deep tropics. Birch et al. (2016) used 10 years of regional climate model simulations over the western MC and found that the interaction between large-scale and mesoscale processes explains the differences in the land-ocean rainfall anomalies associated with the MJO. Using the convection-permitting scale (3 km) simulations, Wei et al. (2020) found that the MJO affects diurnal rainfall characteristics over the MC through modulating both large-scale and local circulation and convection. Convection permitting models are also used to understand the physical mechanisms driving rainfall propagation, which is a key aspect of rainfall diurnal cycle. Over the deep tropics, rainfall propagates offshore due to the convergence caused by the land breeze (Hassim et al., 2016; Coppin and Bellon 2019, Peatman et al., 2023), density currents from cold pools (Mori et al. 2004; Dipankar et al., 2019) and diurnally forced gravity waves (Love et al., 2011; Hassim et al., 2016). Previous studies also found that precipitation propagation near and far from the coast may be driven by different physical mechanisms (Vincent and Lane, 2016; Peatman et al., 2023). For example, Peatman et al. (2023) demonstrated that rainfall moves approximately 150-300 km offshore at a speed comparable to that of land breeze density current, while gravity waves initiate isolated convection cells, which are typically farther from shore and have much weaker rainfall. At higher latitudes, offshore propagation is primarily controlled by large-scale background winds under trapped land-sea breeze circulation conditions (Fang and Du 2022). These studies suggest that kilometer-scale simulations are a useful tool for understanding physical processes across multiple length scales.

Coastal rainfall in northern Queensland is influenced by both large-scale and mesoscale processes, as well as their interactions. However, the physical mechanisms behind these scale interactions remain unclear, primarily due to the lack of convective-resolved simulations. Moreover, most previous studies have focused on the mechanisms driving rainfall propagation in the deep tropics. The mechanisms may differ depending on geographical locations (e.g., coastal regions of Queensland versus the deep tropics) and background meteorological regimes (e.g., easterly trade winds in Queensland), and therefore require further investigation. This study aims to understand the interaction between mesoscale processes and large-scale forcings in modulating coastal rainfall over the northern Queensland using convection-permitting regional atmospheric simulations. We address three key research questions in this study: (1) What is the observed and simulated spatial distribution of local rainfall patterns across coastal northern Queensland? (2) What factors drive the inhomogeneous rainfall patterns along the coast? (3) How do mesoscale processes interact with large-scale forcings in driving rainfall propagation?

2 Model, Data and Methods

2.1. Model experiment

Our study uses convection-permitting regional simulations produced by the AUS2200 project (Huang et al. 2024) – a high-resolution regional modelling framework based on the United Kingdom Met Office Unified Model (UK Met UM) (Brown et al., 2012) with atmosphere version 12.2 and Joint United Kingdom Land Environment Simulator (JULES) (Best et al., 2011; Clark et al., 2011). The third Regional Atmosphere and Land (RAL) science configuration is employed in this framework. This model setup features a grid spacing of 0.0198° (approximately 2.2 km) and 70 vertical levels. As a convection-permitting simulation, AUS2200 explicitly resolves convection, allowing it to develop dynamically rather than relying on parameterization. The simulations employed a large domain that covers the entire Australian continent and some of the surrounding oceans, as shown in Fig. 1a. Previous studies suggest that a large regional domain with kilometer-scale horizontal resolution is necessary to capture the local-scale interactions (e.g., Birch et al., 2013) and to minimizes the influence of edge effects (such as spin-up issues near the boundaries) which can negatively impact precipitation characteristics (Jones et al., 2023). Lateral boundary conditions are updated every 6 hours from the European Centre for Medium-Range Weather Forecast ERA5 Reanalysis (Hersbach et al., 2020). Soil moisture is initialized using data from the Bureau of Meteorology Atmospheric high-resolution Regional Reanalysis for Australia -Version 2 (BARRA2, Su et al. 2022), which is also based on the UK Met UM to improve consistency between the soil moisture initialization and the land-surface in these simulations. The model is run for three MJO events with a well-defined eastward propagation (Fig. S1) under different ENSO conditions: January/February for 2013 (ENSO neutral), 2016 (El Niño) and 2018 (La Niña), with a 24-hour reinitialization and 24-hour spin up. Sea surface temperatures were prescribed daily from the ERA5 data with the horizontal resolution of 0.25°. The simulations were performed with daily reinitialization over a 48-hour period, including a 24-hour spin-up.

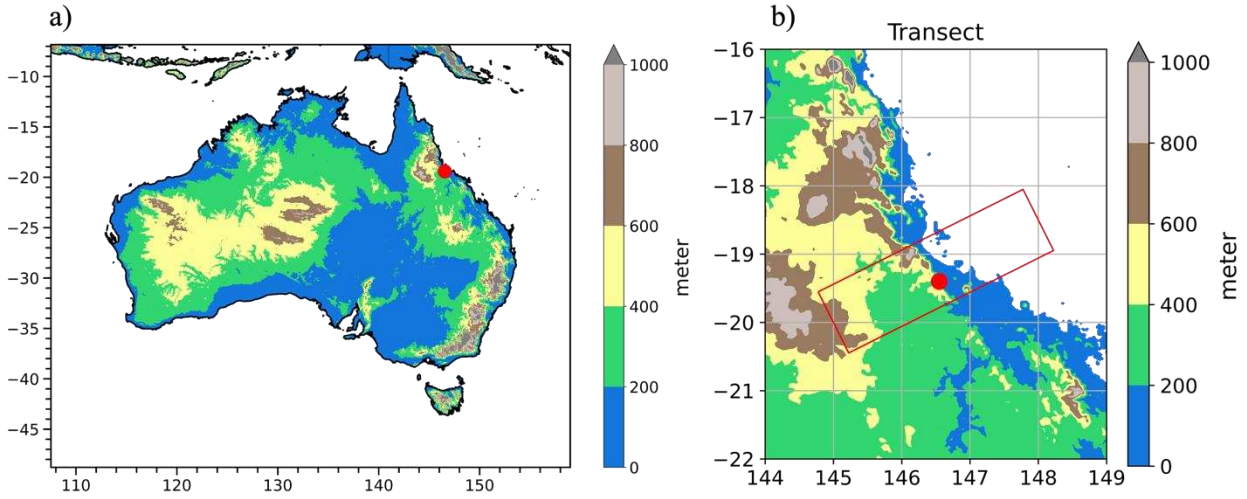

Figure 1. (a) Model domain and orography for the convection-permitting AUS2200 experiment, with the red dot indicating the Townsville radar location used in this study. In (b), the red box denotes the transect used in Figs. 7-8, 10-13.

2.2. Observational and reanalysis datasets

Different datasets are utilized to understand the coastal rainfall features and to evaluate the model simulations. Daily rainfall data from the Australian Gridded Climate Data (AGCD) version 1, with a horizontal resolution of 0.05° x 0.05° (Jones et al. 2009), is used to evaluate the simulated daily rainfall patterns and their variation with large-scale climate variability over Northeast Australia. This dataset has been widely used to examine the precipitation variability in Australia (King et al., 2013; Black and Lane 2015; Ghelani et al., 2017; Dao et al., 2023). Radar-derived rainfall is used to analyze observed coastal rainfall, rainfall propagation and to evaluate simulated rainfall patterns at small scale. Radar data is from the Australian Unified Radar Archive level 2 "Rain Rate" datasets, which has a horizontal resolution of 1 km, covering a radius of up to 150 km from the radar location (Soderholm et al., 2022). We used a modern S-band Doppler radar located in Townsville, a coastal area of north Queensland (Fig.1). Using this radar, Dao et al. (2025) demonstrated that rainfall over Townsville is strongly influenced by both large-scale variability (e.g., MJO) and local variability (e.g., land-sea breeze circulation). A detailed description of the radar rainfall retrieval and quality control applied to the level 2 datasets can be found in Dao et al. (2025). Precipitation estimates from radar reflectivity and the Global Precipitation Measurement (GPM) Integrated Multi-satellite Retrievals for GPM-IMERG are used to evaluate precipitation on a diurnal timescale. The GPM-IMERG dataset has half-hourly temporal resolution with a global horizontal resolution of 0.1° x 0.1° (Huffman et al. 2019).

The 850-hPa atmospheric wind, obtained from the Bureau of Meteorology Atmospheric high-resolution Reanalysis for Australia-Version 2 (BARRA2) reanalysis data (Su et al., 2022) is used to examine the atmospheric circulation over the entire study period and for different MJO phases, as well as to evaluate the wind field in AUS2200 simulations. Upper-air radiosonde sounding data for Townsville station obtained from the University of Wyoming data archive is used to examine wind vertical profiles for different categories of rainfall propagation. The analysis is based on soundings at 00 UTC (corresponding to 10 a.m. local time (LT)) with all sounding data interpolated to standard pressure levels.

2.3. Methods

To examine the variation of coastal rainfall over northern Queensland, a total of 180 simulation days for three MJO events are analyzed in this study. The Real-time Multivariate MJO (RMM) index (Wheeler and Hendon, 2004, hereafter WH04) is used to classify the MJO phases. MJO events (Fig. S1) are selected during the austral summer (DJF) based on two criteria: (1) The amplitude of the RMM index should be equal to or greater than 1, and (2) the MJO propagates through 8 phases. Coastal rainfall is classified into five different groups based on its spatially averaged rainfall (Table 1), to better distinguish the various coastal rainfall patterns in northern Queensland. The 90^{th} and 20^{th} percentile thresholds are first applied to categorize days into heavy rain and less rain groups, respectively. The remaining days are then classified into three typical coastal rainfall patterns (LAND, OCEAN, COAST), which are likely driven by different physical processes (Birch et al., 2016; Vincent and Lane 2017; 2018), using average rainfall areas. For example, the land group includes days when the average rainfall over land exceeds the average rainfall over the coast and ocean areas. In this study, the coastal area is defined as extending 0.5° from the coastline both seaward and landward. Rainfall propagation is subjectively classified into three groups: OFFSHORE PROPAGATION, ONSHORE PROPAGATION, and NO PROPAGATION, based on the Hovmöller diagrams. The offshore

group includes days when rainfall exhibits a clear and distinct diurnal cycle with offshore propagation. The onshore group includes days when rainfall occurs over the ocean and subsequently propagates onshore. The no propagation group encompasses days when rainfall occurs and remains over land throughout the day. The rainfall propagation speed is estimated using a diurnally averaged Hovmöller diagram by finding the best-fit line connecting the longitudes of maximum precipitation rate at each time step. Although an algorithmic approach to classify rainfall propagation would be optimal, its complexity makes it less feasible for this study. Given the limited number of days analysed in this study, a subjective classification offers a more practical and efficient approach.

Table 1: Definition of rainfall groups classified in this study. R is the average rainfall over the entire study area. R_{land}, R_{ocean}, R_{coast}, are the average rainfall over land, ocean and coast, respectively. The classification of R_{land}, R_{ocean}, R_{coast} are conducted after excluding the days from the first two groups (LESSRAIN and HEAVYRAIN).

Type of classification	Criteria
LESSRAIN	$R < 20^{th}$ percentile
HEAVYRAIN	$R > 90^{th}$ percentile
LAND	$R_{land} > R_{ocean}$ and $R_{land} > R_{coast}$
OCEAN	$R_{ocean} > R_{land}$ and $R_{ocean} > R_{coast}$
COAST	$R_{coast} > R_{ocean}$ and $R_{coast} > R_{land}$

3 Results

3.1 Spatial distribution of coastal rainfall.

This section examines the rainfall patterns in northern Queensland and their variation associated with large-scale climate variability in observations and the AUS2200 model simulations for the full study period, which consists of January and February of three distinct years. Figure 2 compares the spatial distributions of daily mean rainfall and low-level winds between observations (Fig. 2a) and model simulations (Fig. 2b). The observed precipitation exhibits a clear geographical variation, with higher amounts (approximately 8-10 mm/day) concentrated in the deep tropics and along the coast. Predominantly onshore, southeasterly winds, which are a key synoptic feature of Queensland's rainfall climate (Kingaman et al., 2012), are also observed across the study domain. The AUS2200 simulations reproduce well these key observed features of rainfall and wind circulation, with a spatial correlation of 0.89 between observed and simulated precipitation patterns. Note that both observed and simulated results are regridded to 25 km, so the validation is not including the smallest scales of variability. This resemblance suggests that the model simulation effectively captures the influence of wind on precipitation dynamics, as easterly winds transporting moisture from the Coral Sea can lead to heavy rainfall when they encounter the Queensland coastal regions due to local-scale interactions (Gillett et al., 2023). Minor biases, ranging from -1 to 1 mm/day, are distributed across the domain, indicating that AUS2200 simulates observed rainfall reasonably well in a mean sense (Fig. 2c). Both the magnitude and distribution of these errors are more localized, despite some underestimation (blue spots) and overestimation (red spots) in certain areas of far north Queensland. While there are westerly biases over the Cape York peninsula and northerly biases

over the western part of Queensland, there appears to be good agreement between observed and simulated precipitation and wind around the Townsville radar area (19.42°S, 146.55°E), which will be the focus of subsequent analyses. In this region, the model simulation achieves relatively high Spearman correlation coefficients, and low mean absolute error (MAE) and root-mean-squared error (RMSE) values (Fig. S2) indicating reliable performance in simulating the rainfall patterns.

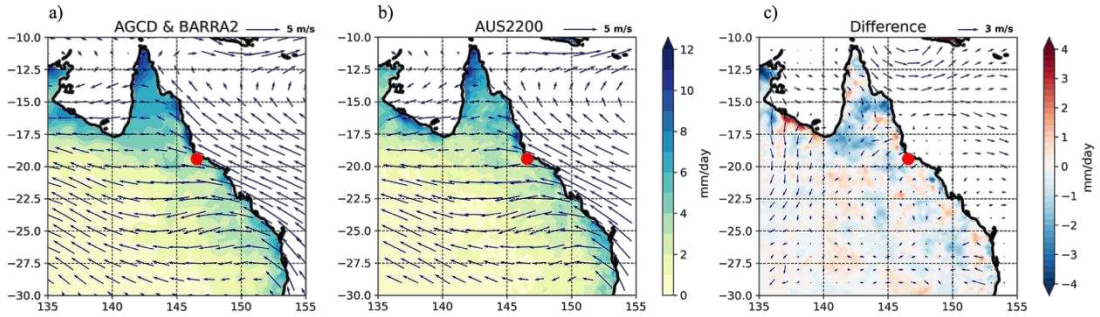

Figure 2: (a) The spatial distribution of daily rainfall (unit: mm/day) from AGCD and 850 hPa wind (unit: m/s) from BARRA2 during the entire study period (January-February for 2013, 2016 and 2018), (b) as in (a), but for AUS2200 simulations, regridded to 25 km, and (c) the difference between (b) and (a). The red dot indicates the Townsville radar location.

Even though our study with a total of 180 days is limited in temporal representativity, it still reflects some key climatological features of the MJO-rainfall relationship in Queensland (Fig. 3). Despite smaller amplitudes compared to observations, the signals of widespread increased rainfall over the tropics during the enhanced convection phases and localized increased rainfall along the coast during the suppressed convection phases of the MJO are evident in the model simulations. In addition, both observations and model simulations clearly show changes low-level circulation during different MJO phases (Fig. S3). These variations are consistent with previous studies (Dao et al., 2023 and Dao et al., 2025), who used longer data period to examine the influence of the MJO on rainfall over NE Australia. The model simulation captures fairly well the spatial variability of wind patterns across the domain and their temporal variations with MJO phases, which is an expected result since the ERA5 controls the large-scale conditions at the boundaries of model experiments. These results indicate that the AUS2200 simulation successfully simulates the timing of the wet and dry phases of the MJO. The most obvious difference between observations and model simulations occurs in phase 8 of the MJO for the three MJO cases studied here. In this phase, locally enhanced rainfall signals along the coast are evident in the model simulations but not in the observations. Furthermore, the model simulation fails to accurately simulate the low-level wind field over the tropical and coastal land areas during this phase. These differences warrant further investigation, but are not the focus of this study.

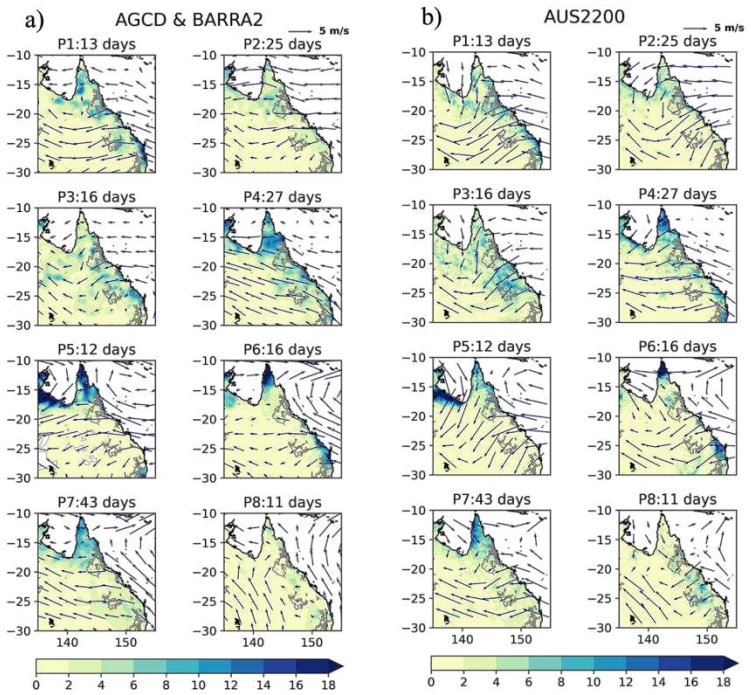

Figure 3: (a) Composites of daily rainfall (shading, unit: mm/day) from AGCD and 850-hPa wind (vectors, unit: m/s) from BARRA2 during the experimental period (January-February for 2013, 2016 and 2018) in eight different MJO phases according to the RMM index (WH04). (b) as in (a), but for AUS2200 simulations. Only days with amplitude of the RMM index greater than or equal to 1 are selected for the analysis. The number of days for the corresponding MJO phase is shown in the top of each panel. Grey contour lines show the altitude of orography above 500 m.

Figure 4 presents the precipitation patterns derived from radar data and the AUS2200 simulations over northern Queensland's coastal areas, categorized into the five distinct groups described in Table 1. Since the classification is applied for radar and AUS2200 data separately, the days included in each group between radar observations and AUS2200 simulations are not necessarily the same. The highest agreement occurs in the land group, where approximately 70% of the days match between the radar observations and AUS2200 simulations, while the lowest percentage, about 40%, is found in the coast group. In the radar observations, the ocean group, where the greatest rainfall is observed over the ocean, is the most frequent pattern, accounting for approximately 35% of the total days. Both the land and coast groups also account for more than 20% of the days. This indicates that observed coastal rainfall in northern Queensland is spatially inhomogeneous, and therefore there is a need to understand the physical mechanism driving each distinct rainfall pattern. The AUS2200 simulation successfully captures rainfall pattern for most of the categorized rainfall groups, except for the coast group. In the model simulations, the ocean group remains the most frequent rainfall pattern, including about 30% of the total days. The AUS2200 simulation tends to overestimate rainy days over land while underestimating those over the ocean and coastal regions. At this finer scale, larger discrepancies appear between observed and simulated rainfall patterns. For example, in the coast group, radar observations indicate higher rainfall over the southern coast of the radar domain, while the AUS2200 simulates more rainfall over the northern coast. Rainfall concentrated near the coast is

likely influenced by multiple processes, which could explain the model's challenges in capturing the correct pattern.

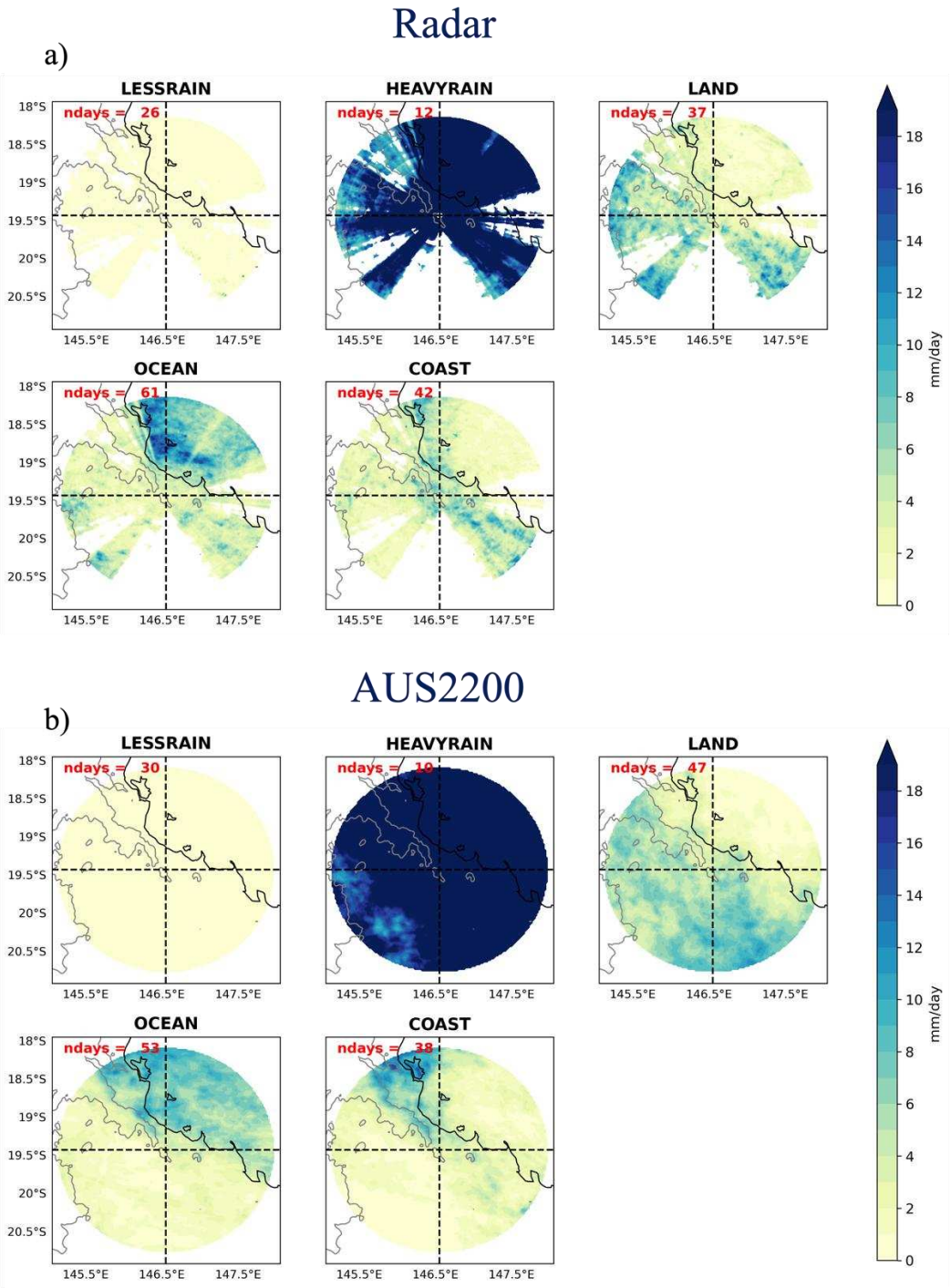

Figure 4: The spatial distribution of rainfall in different categories during the experimental period (January-February for 2013, 2016 and 2018) over the coastal regions of Queensland for

(a) radar observations and (b) AUS2200 simulations. Days of model and radar data are considered separately. The number of days for the corresponding rainfall group is indicated in the top left of each panel. Areas with high beam blockage fraction are filtered out in radar observations.

The above results demonstrate that coastal rainfall in northern Queensland is spatially inhomogeneous and potentially driven by different physical processes. Previous research suggested that rainfall propagation can be a critical factor in determining total precipitation distribution over coastal areas (Coppin et al., 2020). As the aim of this study is not only to understand the spatial distribution of rainfall, but also to investigate the causes of these observed rainfall patterns, we next examine the average coastal rainfall patterns associated with different rainfall propagation groups. The rainfall propagation groups are classified into three groups using the method introduced in Section 2.3: offshore propagation group, onshore propagation group, and no propagation group (Fig.5). Note that there were days that did not fall into any propagation group. Each type of rainfall propagation will be discussed in detail in the next section. Radar observations indicate that different propagation types exhibit distinct rainfall patterns (Fig. 5a) that resemble those shown in Fig.4. The offshore rainfall group displays widespread rainfall signals across the entire radar domain. In contrast, the onshore rainfall propagation shows the highest rainfall intensity over the ocean, while the no propagation group exhibits greater rainfall over land. Notably, the offshore rainfall group demonstrates stronger rainfall intensity compared to the other two groups. The AUS2200 simulation successfully captures both the spatial distribution and intensity variations of rainfall across the three different propagation groups (Fig. 5b). The number of days in each group is also comparable to the observations, although they are not necessarily the same days. In summary, both observational and model results suggest that rainfall propagation modulates average rainfall pattern over the coastal areas of northern Queensland. Therefore, understanding the physical mechanisms driving different rainfall propagation types can help explain the causes of the inhomogeneous rainfall patterns along the coast.

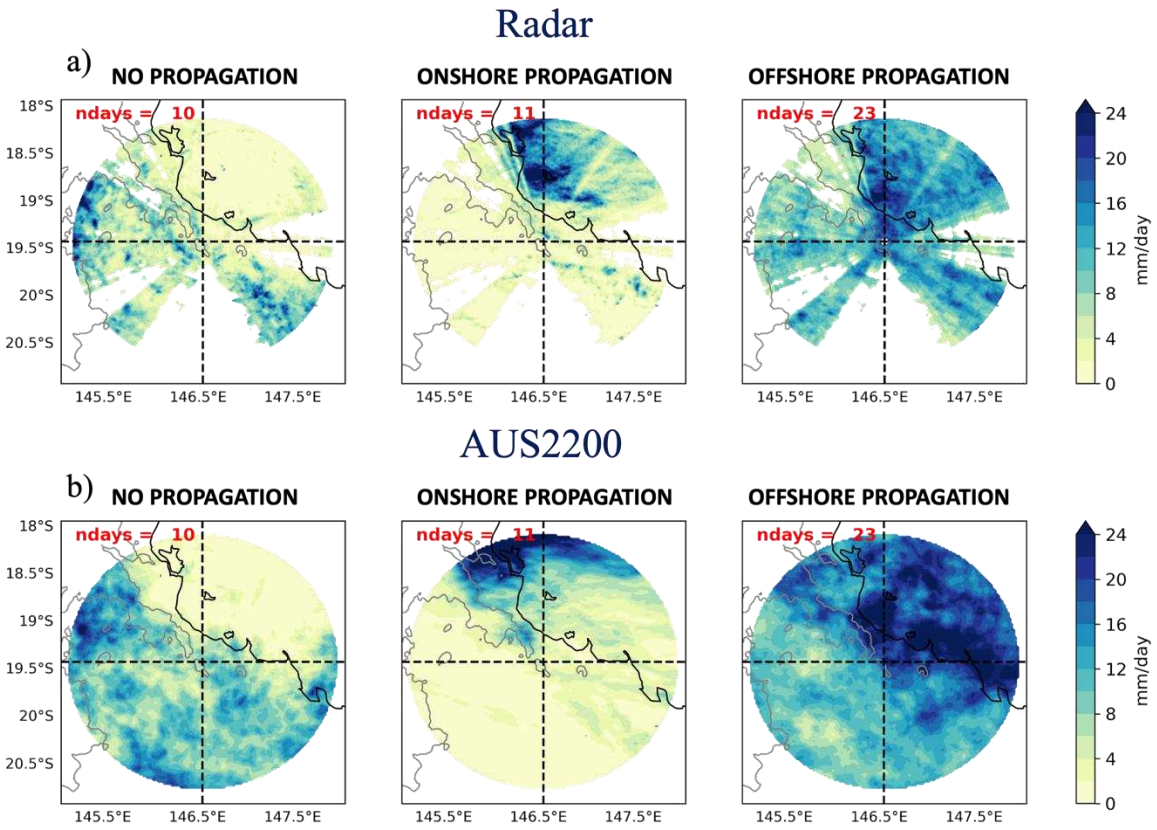

Figure 5: The spatial distribution of average precipitation for different propagation groups during the experimental period (January-February for 2013, 2016 and 2018) over the coastal regions of Queensland for (a) radar observations and (b) AUS2200 simulations. The number of days for the corresponding propagation group is indicated in the top left of each panel. Note that only days showing the consistency between observations and model simulations are presented

3.2. Physical mechanisms behind inhomogeneous coastal rainfall patterns.

This section uses model simulations to investigate the physical processes driving rainfall propagations. Thus, only the days showing consistency between observations and AUS2200 simulations are included in the analysis.

3.2.1. Offshore rainfall propagation

We first examine the offshore rainfall propagation, which is the most frequent type of propagation in northern Queensland. There is good agreement between the satellite and radar data in capturing the offshore rainfall propagation (Fig. 6a). Rainfall typically initiates over land during the afternoon local time and propagates offshore into adjacent coastal waters at night. There are notable differences in rainfall propagation patterns between 2013 (ENSO neutral), 2016 (El Niño) and 2018 (La Niña). For example, during the dry El Niño conditions, offshore rainfall events tend to be weaker in intensity compared to those observed during neutral and wet La Niña conditions. In the AUS2200 simulations (Fig. 6b), there is an underestimation of rainfall intensity compared to the observations for most days. One possible reason is that the simulation

tends to underestimate heavy rainfall events, which occur more frequently during offshore rainfall propagation. However, we select these consistent days (23 days) as they capture the key features of offshore rainfall propagation. The AUS2200 successfully simulates the propagation of rainfall from land in the afternoon to the ocean at night. Additionally, the variation in precipitation intensity across different climate conditions (e.g., El Niño, La Niña) is also obvious in the model simulation, indicating that our results span a range of background climate states.

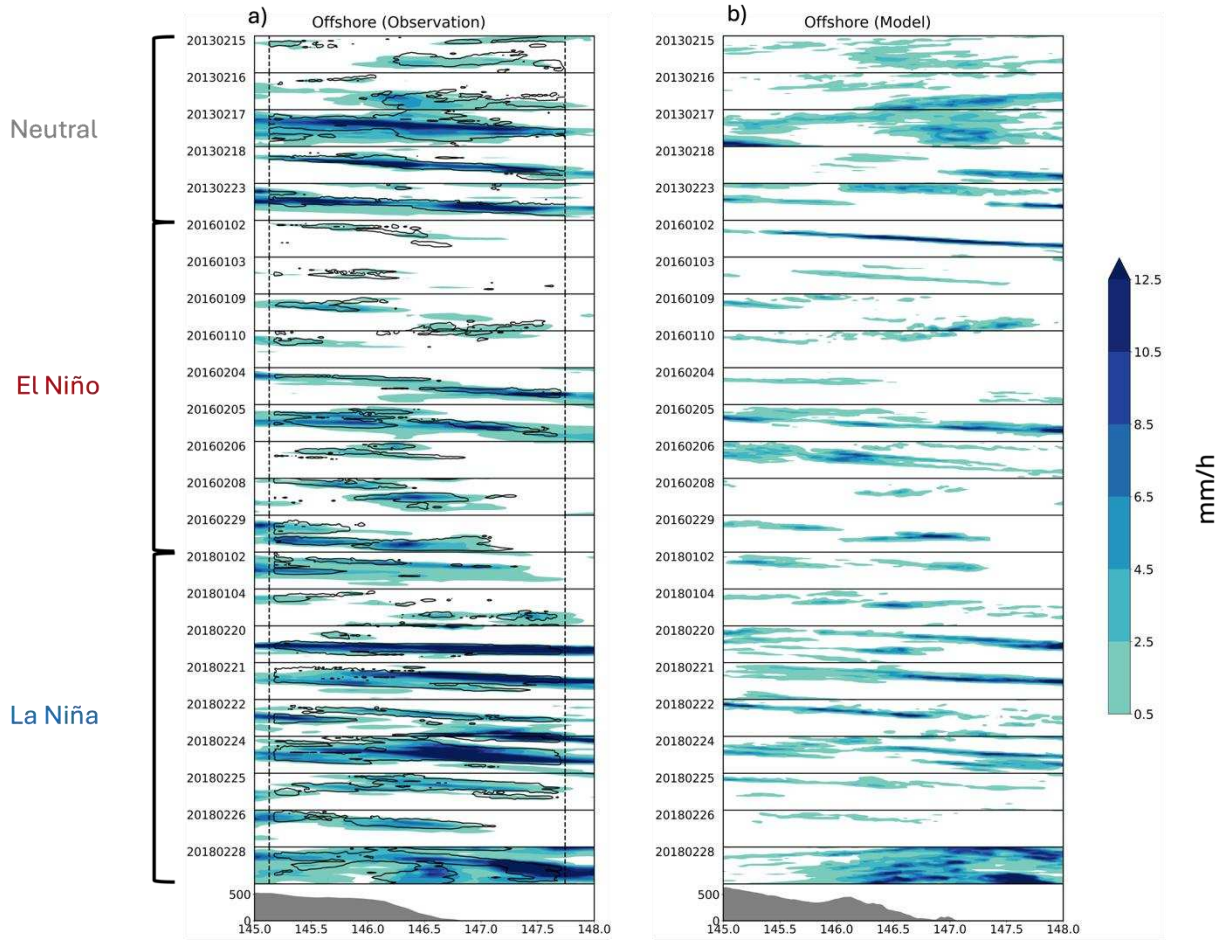

Figure 6: Hovmöller diagrams of rainfall rate for offshore propagation days during the experimental period (January-February for 2013, 2016 and 2018) along the transect shown in Fig. 1b for (a) GPM IMERG (shading) overlaid with radar (black contours showing 0.5 mm/h) and (b) AUS2200 simulations. The horizontal grid lines are at 00:00 UTC (10:00 LT), with longitude shown along the horizontal axis. Dashed black vertical lines show the range of the radar transect. The average topography across the transect is indicated in blue below each panel. Topography data is obtained from ERA5 and AUS2200 for (a) and (b), respectively. Note that only days showing the consistency between observations and model simulations are presented.

To investigate the physical mechanisms of offshore rainfall propagation, we examine the average vertical cross-sections for all days presented in Fig. 6 from the AUS2200 simulations (Fig.7). Upper-and mid-level westerlies (above 2 km) are consistently present throughout the day across the entire domain. At lower levels (below 1.5 km), easterly winds are observed all day,

but with notable variations in their strength, suggesting the presence of land-sea breeze circulation. These easterly winds reflect the prevailing trade wind regime superimposed with the sea breeze perturbation, but with no full flow reversal to westerly surface winds under nighttime or early morning land breeze conditions. By local noon (13 LT), the sea breeze flows onshore, generating upslope flow over the topography and low-level moisture convergence near the coast (MFC, red curve on lower panel). The sea breeze continues to propagate further inland and interact with large-scale background westerlies. These processes lead to rainfall associated with low-level convergence over the land indicated by surface rain rates (blue curve on the lower panel), as well as the mixing ratio vertical profiles of clouds (orange contours on the upper panel) and precipitation (blue contours on the upper panel), as well as the mixing ratio vertical profiles of clouds. As the sea breeze intensifies and extends farther inland by 16 LT, deep convection is triggered over land, which contributes to higher rainfall values (blue curve on the lower panel) and low-level convergence (red curve on the lower panel). During the nighttime (22 LT – 7 LT), the low-level easterly flows weaken and retreat toward the ocean. At the same time, rainfall also propagates offshore within the radar domain. High surface rainfall rate (approximately 1.5 mm/hour) and low-level moisture convergence are observed over the oceanic coast at 22 LT. Rainfall continues to propagate offshore from the coast with the weakening of low-level easterlies and the persistence of strong westerly winds above. Surface rain rates and low-level moisture convergence is observed mostly over the ocean from 1 LT to 7 LT. Clouds and precipitation (orange and blue contours on the upper panel) are also concentrated over the ocean during this period. The weakening of low-level easterlies during the night and early morning indicates the presence of land breezes, manifesting as a westerly anomaly but not an actual reversal of the wind direction, that can contribute to drive rainfall offshore. This is consistent with Peatman et al. (2023), who found that in their selected case studies, rainfall over Sumatra propagates approximately 150-300 km offshore with the land-breeze density current.

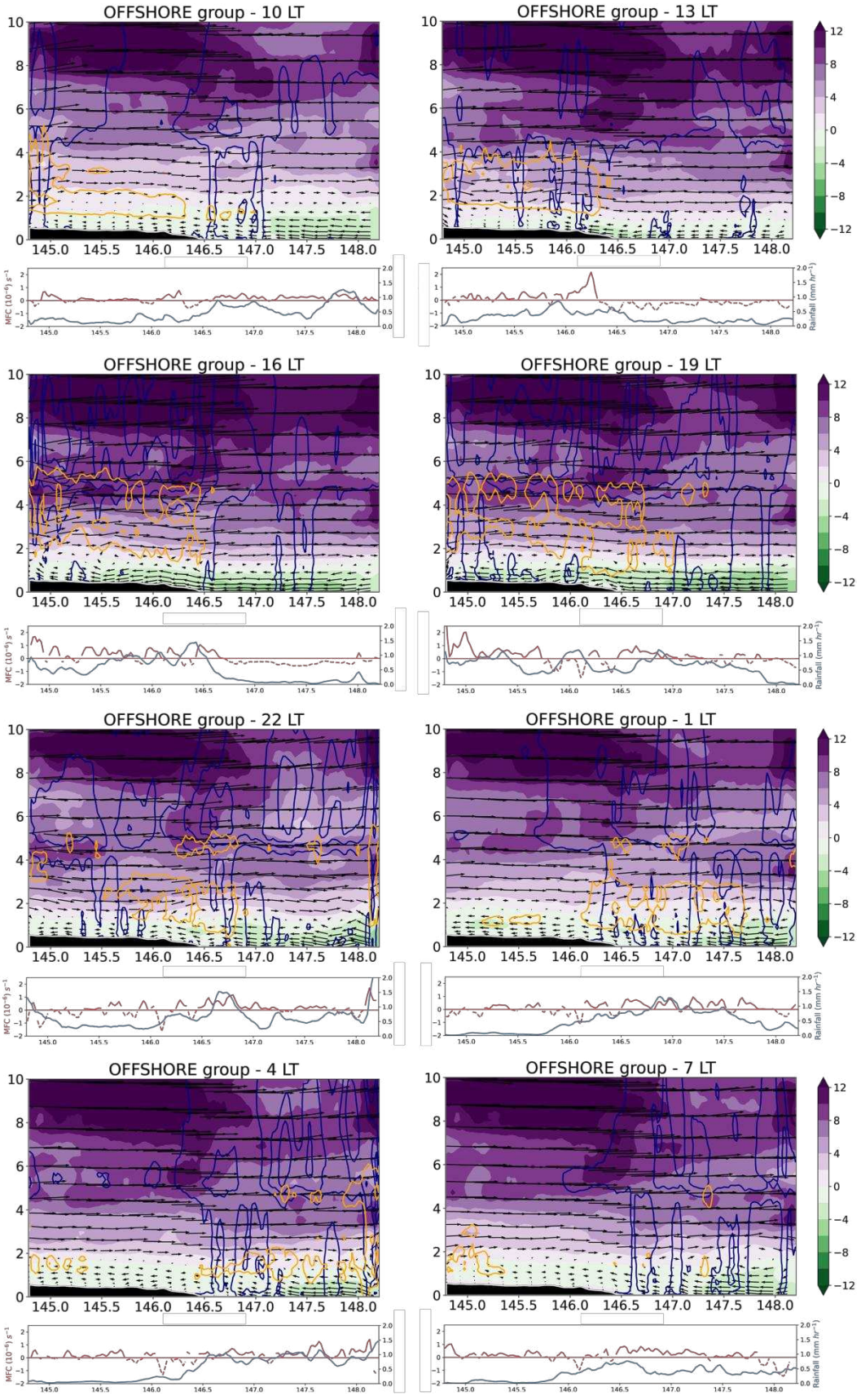
OFFSHORE group - 10 LT
OFFSHORE group - 13 LT
OFFSHORE group - 16 LT
OFFSHORE group - 19 LT
OFFSHORE group - 22 LT
OFFSHORE group - 1 LT
OFFSHORE group - 4 LT
OFFSHORE group - 7 LT
MFC (10^{-6}) s^{-1}
Rainfall (mm hr^{-1})

401

Figure 7: Average vertical cross sections at selected times for offshore propagation group, showing zonal and vertical wind (vectors, with zonal wind also in colored shading, unit: m/s), mixing ratio of cloud liquid (orange contours, unit: kg/kg, levels: 0.4 to 2 with an interval of 0.4), mixing ratio of rain+ graupel + snow (blue contours, unit: kg/kg, levels: 0.4 to 4 with an interval of 0.8), topography (black), rain rate (blue curve, unit: mm/h), and along-transect moisture flux convergence (MFC) averaged over 0-500 m above sea level (red curve, unit: kg/kg/s, solid for convergence and dashed for divergence). The figure was plotted following Peatman et al. (2023).

We next examine the relationship between rainfall propagation speed and the average wind speed at different height levels. Wind speed for each day is averaged over the period when rainfall occurs along the transect indicated in Fig 1b. The averaged rainfall propagation speed across all day in the group is approximately 5 m/s. We examined the influence of wind on rainfall propagation speed at different height levels, ranging from the surface up to 8 km above topography, and found a strong correlation between rainfall propagation speed and wind speed at two specific height levels: 0-1 km and 1-2 km (Fig. 8). At the 0-1 km level (Fig. 8a), the wind direction alternates between easterlies (11 days) and westerlies (8 days) during offshore propagation days, which explains why a diurnal wind reversal is not visible when averaging over all days. The correlation between rainfall propagation speed and wind speed reaches 0.58 at this level, suggesting that the land breezes play a role in driving rainfall offshore. The strongest correlation (0.65) between rainfall propagation speed and wind speed is observed at the 1-2 km level (Fig. 8b). At this height, most days show westerly wind, indicating that large-scale background westerlies just above the boundary layer play a crucial role in driving rainfall offshore or in slowing its offshore propagation in the case of the easterly winds. This suggests that the migration of surface convergence from the land-sea breeze circulation and/or cold pools dynamics is more important than the mid-level steering flow in controlling the offshore rainfall propagation.These results are consistent with those shown in Fig. 7, highlighting the role of both land breeze and large-scale background winds in driving rainfall offshore over coastal areas of northern Queensland, probably with a more substantial influence from large-scale westerlies. Rainfall propagation speeds in this study (2-8 m/s) are consistent with the near-shore part of the offshore propagation found in the deep tropics by Peatman et al. (2014), Vincent and Lane (2016). We do note that the rainfall propagation speed is faster than the wind speed, and we do not imply that the coastally aligned squall line is simply being advected by the winds. Indeed, the propagation speed is likely a combination of factors including the steering flow, the speed of the density current, which is linked to the strength of the negative buoyancy forcing associated with the land-sea temperature difference, and the possible reinforcement of this density current by the cold pools associated with the offshore propagation convection.

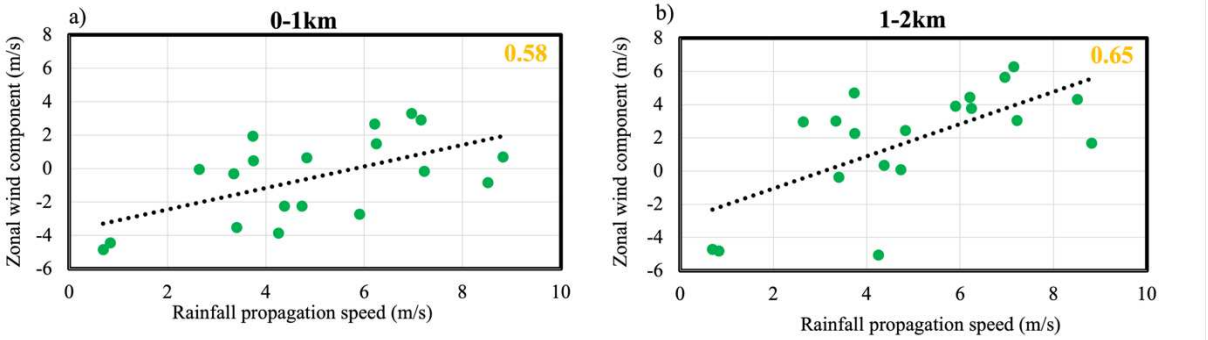

Figure 8: The relationship between rainfall propagation speed and average wind speed along the transect for (a) 0-1 km and (b) 1-2 km above the topography for the offshore propagation group from AUS2200 simulations. The correlation coefficient between wind speed and rainfall propagation speed is indicated in the top right of each panel. Trend lines (black) are also included.

3.2.2. Onshore rainfall propagation

Similar to the offshore propagation group discussed in the previous sections, the Hovmöller diagrams of observed and simulated rain rates for onshore rainfall propagation are presented in Fig. 9. Focusing on the days when both observations and model simulations show consistency, a total of 11 rainy days are classified as onshore propagation in both the observations and AUS2200 simulations. In the observations, radar results generally align well with satellite results, indicating that rainfall typically initiates over the ocean and propagates onshore. Discrepancies between radar and satellite data are observed on certain days (e.g., 20130106, 20130211, 20160114, 20180205), most of which exhibit weak and scattered rainfall signals. In addition to capturing the propagation features, which is the main criterion for selecting consistent days between observations and model simulations, the AUS2200 simulation also reasonably simulates rainfall intensity for the onshore propagation group. Overall, the model simulation performs better in capturing rainfall intensity for the onshore propagation group

compared to the offshore group, where it tends to underestimate the rainfall intensity (see Figs. 6 and 9 for comparison).

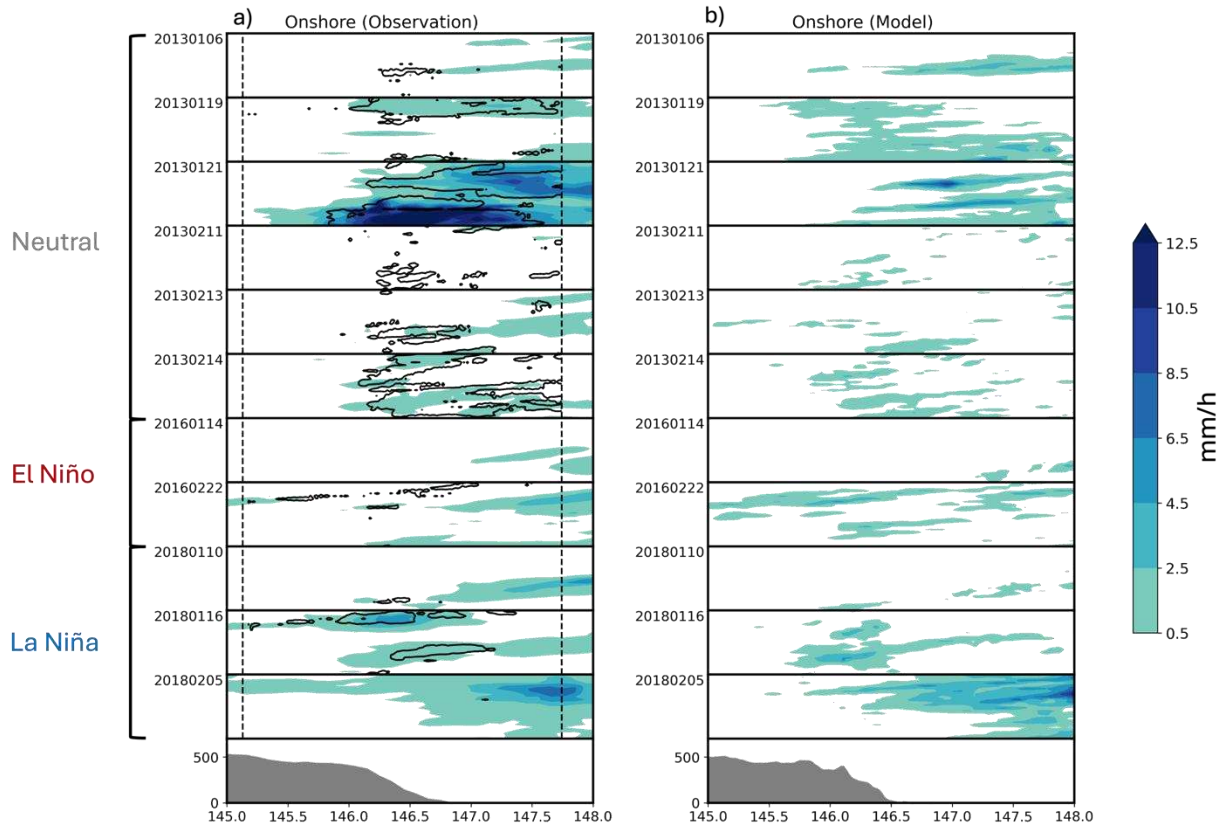

Figure 9: Same as in Fig. 6, but for onshore propagation days

Figure 10 presents the average vertical cross-section for the onshore propagation group based on AUS2200 simulations. For this group, the most striking difference in the wind patterns compared with the offshore case is the dominance of deep large-scale easterly winds, extending from the surface up to 6 km, throughout the day. In the morning (10 LT), rainfall primarily concentrates over the ocean, as indicated by the positive surface rain rate (blue curve in the lower panel) and low-level moisture convergence (red curve in the lower panel). In the atmosphere, low-level clouds (orange contours in the upper panel) are widely distributed across the domain, but precipitation (blue contours in the upper panel) is only observed over the ocean. During the afternoon (13 LT–19 LT), rainfall propagates onshore, as evidenced by both the surface rain rate and the cloud and rain fractions in the atmosphere. By evening (19 LT), the highest rainfall amounts associated with low-level moisture convergence occur over the coastal land possibly due to the interaction of large-scale easterlies wind with topography and frictional convergence. An intensification of background easterly wind occurs after 19 LT, possibly associated with the later onset of the land-sea breeze circulations. This feature is evident in the wind anomaly field (not shown). Note that onshore propagation group has drier and cooler atmospheric conditions over the land compared to other groups, which possibly prevents rainfall from propagating further inland (Fig. S4). During nighttime and early morning, rainfall remains over the ocean or shifts slightly offshore.

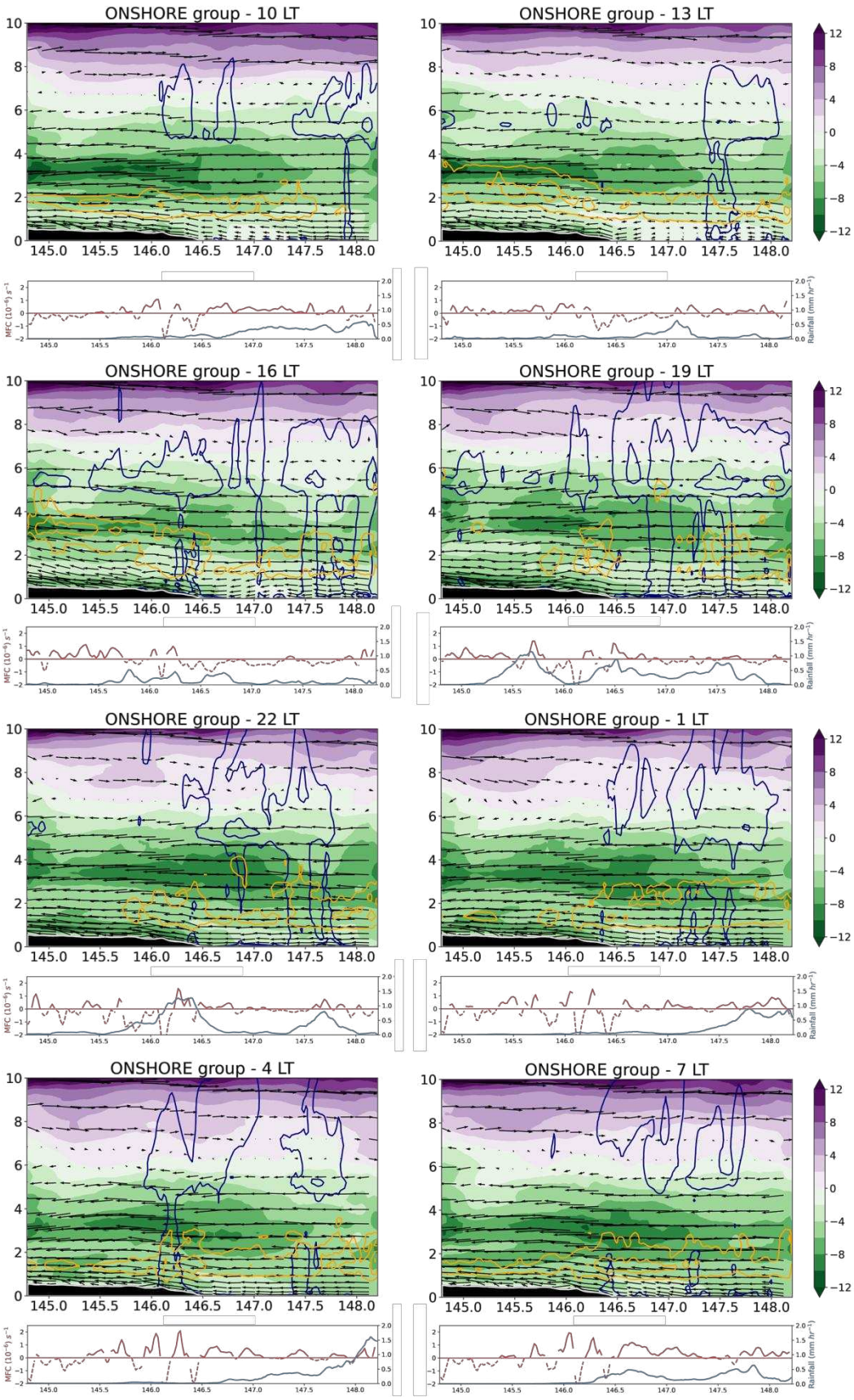
ONSHORE group - 10 LT
ONSHORE group - 13 LT
ONSHORE group - 16 LT
ONSHORE group - 19 LT
ONSHORE group - 22 LT
ONSHORE group - 1 LT
ONSHORE group - 4 LT
ONSHORE group - 7 LT
MFC (10^{-5}) s^{-1}
Rainfall (mm hr^{-1})
u
v

480

Figure 10: Same as in Fig. 7, but for onshore propagation day

The relationship between rainfall propagation speed and the average wind speed is also examined for onshore propagation group (Fig. 11). Different from the offshore propagation group, the results show that the mid-level winds exhibit the highest correlation (above 0.5) with onshore rainfall propagation. At these height levels, most days are characterized by easterly winds. This is consistent with the results shown in Fig. 10 and further suggests that mid-level easterly winds play an important role in driving onshore rainfall.

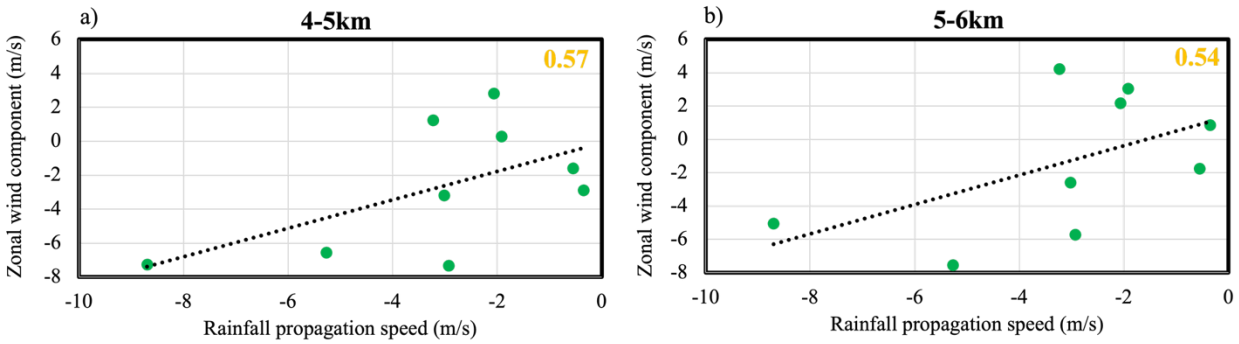

Figure 11: The relationship between rainfall propagation speed and average wind speed along the transect for (a) 4-5 km and (b) 5-6 km above the topography for the onshore propagation group from AUS2200 simulations. The correlation coefficient between wind speed and rainfall propagation speed is indicated in the top right of each panel. Trend lines (black) are also included.

3.2.3. No rainfall propagation

The no rainfall propagation group consists of days when rainfall occurs and remains over land throughout the day. This group is associated with higher average rainfall over the land part of coastal areas (see Figs. 4 and 5). Similar to the previous two groups, a set of Hovmöller diagrams for the no propagation group is presented in Fig. 12. Most days in this group demonstrate that rainfall initiates in the afternoon and persists over land without a clear propagation pattern. Observational data also shows that rainfall intensity is relatively high for the no propagation group, with most days showing rain rates exceeding 10 mm/h. A total of 10 days are classified as consistent between observations and AUS2200 simulations. For these days, the simulation generally captures the rainfall pattern as well as its variation across different days (Fig. 12b). Notably, the observed onset time of precipitation is reasonably well represented in the model simulations for the no propagation group. However, similar to the offshore propagation

group, the AUS200 simulation tends to underestimate the rainfall intensity for the no propagation group.

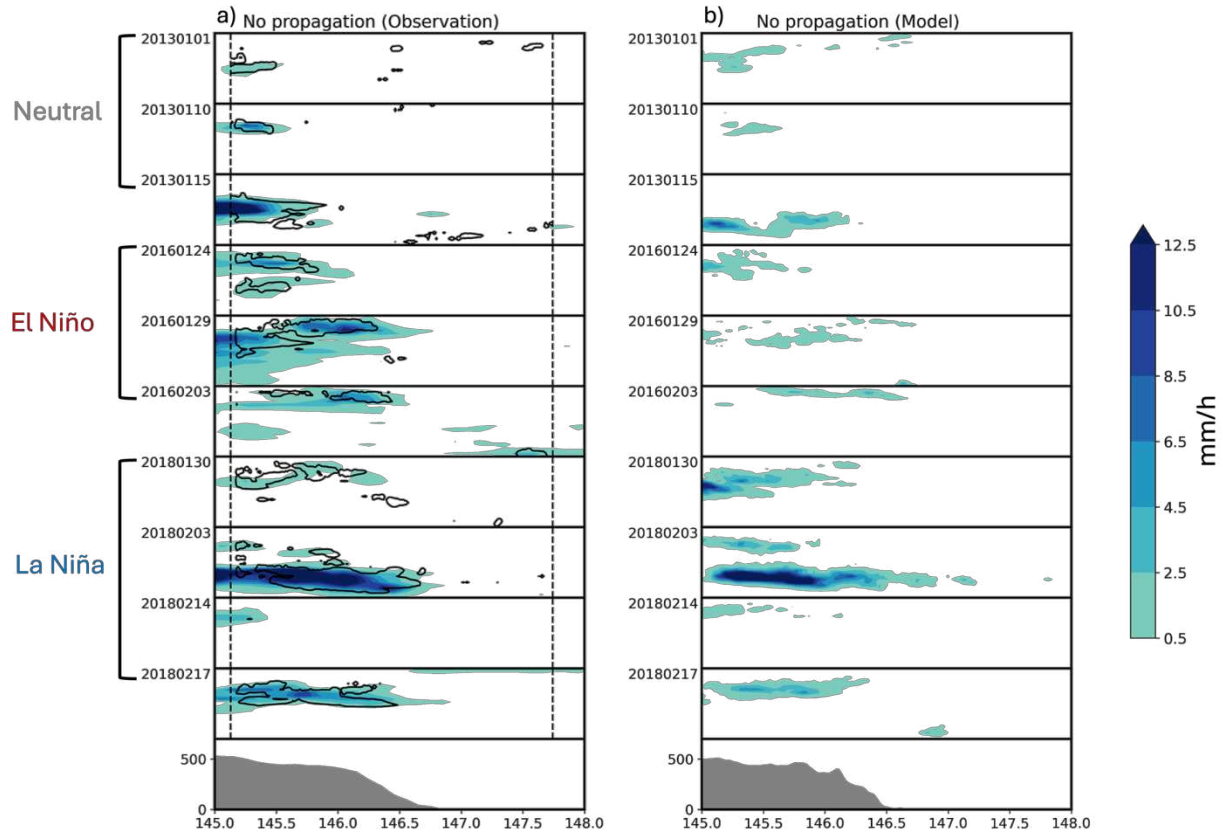

Figure 12: Same as in Fig. 6, but for no rainfall propagation group.

Average vertical cross-sections for the no propagation group from AUS2200 simulations are presented in Fig. 13. In the morning (10 LT), the domain is dominated by low-level westerlies, mid-level easterlies and upper-level westerlies. No rainfall or cloud formation is observed at this time. By early afternoon (13 LT), sea breezes begin to develop, evidenced by the upslope flow and moisture flux convergence (MFC, red curve on lower panel) near the coast. The upslope thermotopographic flows that develop at the same time, can couple with the inland propagation of the sea breeze. Similar results are observed in a cross-section analysis conducted over another box with lower topography, suggesting that the upslope flows are primarily driven by sea breezes. Cloud and precipitation are also observed in the atmosphere over the land part at this time, but this does not result in surface rainfall (blue curve on lower panel). In the late afternoon (16 LT), the sea breezes intensify and move further inland, interacting with low-level large-scale westerlies. This interaction triggers low-level moisture convergence and deep convection, leading to rainfall over the land. Precipitation and clouds persist over land during the evening and night (19 LT - 4 LT) before dissipating in the early morning. The mid-level easterlies weaken gradually during the afternoon (13 LT- 19 LT). However, during the nighttime (22 LT), an easterly wind layer (extending from the surface up to 3 km) develops over the ocean and extends further inland by early morning. The easterly layer is possibly a result of the re-

establishment of the easterly trade winds following the weakening of the return flow of the sea breeze. The process prevents offshore rainfall propagation, causing the rainfall to remain over the land.

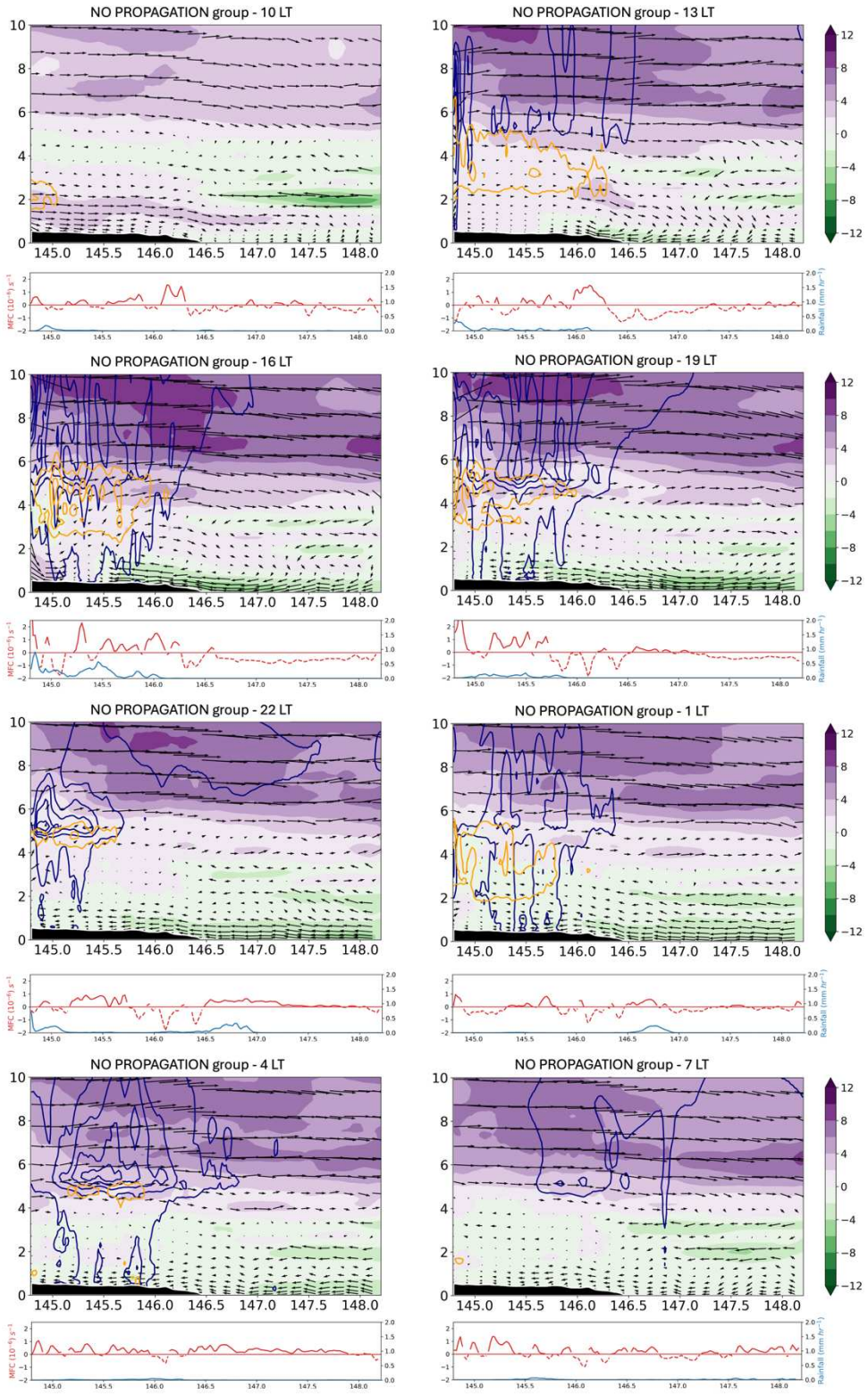

Figure 13: Same as in Fig. 7, but for no rainfall propagation group

The above results suggest that rainfall propagation modulates the average rainfall pattern, leading to spatially inhomogeneous rainfall distributions over coastal areas of northern Queensland. Offshore rainfall propagation, which is the most frequent type, typically leads to a widespread rainfall pattern across the entire coastal radar domain. For this group, rainfall is triggered during the afternoon by sea breezes and propagates offshore during the nighttime with land breezes and large-scale background westerlies. This is consistent with previous studies in the deep tropics showing the influence of land breezes (Vincent and Lane 2016, Birch et al., 2016, Bai et al., 2021 and Peatman et al., 2023) and large-scale background winds (Short et al., 2019, Natoli and Maloney 2022, 2023) in driving offshore rainfall near the coast. In our study, we further find that in Townsville, large-scale backgrounds winds play a greater role compared to land breezes in controlling offshore rainfall. This is consistent with the finding from Fang and Du (2022) demonstrating that outside the deep tropics, the large-scale background winds play an important role in driving rainfall offshore. Onshore rainfall propagation results in a higher rainfall amount over the ocean compared to the land parts of the radar domain. Onshore propagation tends to occur on days with strong and deep easterly trade winds extending from the surface up to 6 km in the atmosphere. Rainfall in this group is associated with the interaction of easterly trade winds and topography, which is a key synoptic-scale process influencing rainfall along the Queensland coast (Lyons and Bonnell, 1992; Connor and Bonnell, 1998, Klingaman, 2012). The no rainfall propagation group is linked to higher average rainfall over the land areas of the radar domain. Sea breezes develop during the afternoon, move inland, and interact with low-level background westerlies, leading to convection and rainfall over land. Rainfall tends to persist over land during the nighttime under the influence of strong easterly winds extending from the surface to the mid-levels of the atmosphere. Note that stronger and deeper sea breezes are observed in the offshore rainfall and no propagation groups compared to the onshore rainfall propagation group (Fig. S5). In addition, the sea breeze signals tend to appear later in the onshore propagation group than in the offshore and no propagation groups. Our results suggest that both large-scale background wind and the local scale land-sea breeze circulation are crucial factors driving rainfall propagation. Any large-scale circulation that modulates background wind regimes is likely to influence rainfall propagation and its associated rainfall patterns along the coast.

3.2.4. Relationship between rainfall propagation and large-scale climate variability

Observational results indicate a clear distinction in the vertical wind profiles among the three rainfall propagation groups (Fig. 14a). Specifically, the offshore propagation group is characterized by weak low-level easterly winds (from the surface to 900 hPa) and upper-level westerlies. In contrast, the onshore propagation group is marked by strong, deep easterlies extending from the surface up to 500 hPa. The no propagation group is associated with low-level westerly winds and mid-level easterly winds (from 800 hPa to 600 hPa). Note that since the soundings are taken from 10 am LT, they should not be strongly influenced by the land or sea breezes. These findings are consistent with the results from the modeled vertical cross-section presented in the previous section, further emphasizing the role of large-scale background winds in controlling various rainfall propagation patterns in Queensland's coastal areas. Note that only days consistent between observations and model simulations (as discussed in section 3.2.3) are presented. However, the results remain similar when considering all observation and modeling days separately (Fig. S6). The AUS2200 simulation effectively captures the shape of the observed vertical wind profiles for the three propagation groups (Fig. 14b). However, the

simulation underestimates wind intensity, leading to the smaller differences in wind profiles among the three propagation groups compared to the observations.

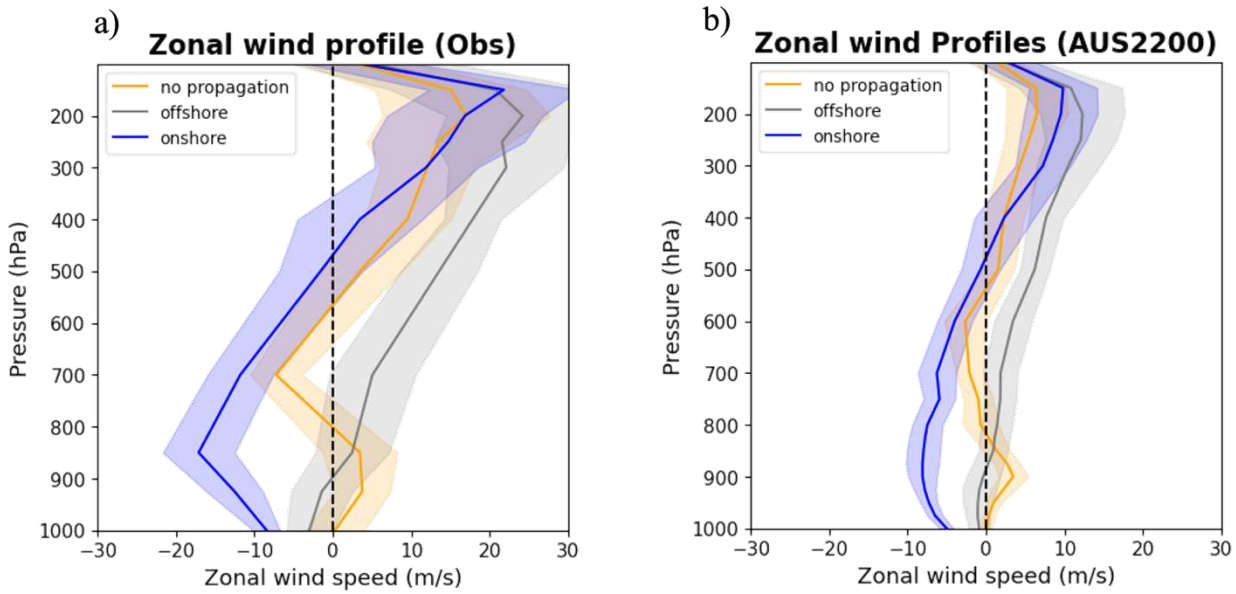

Figure 14: Zonal wind profiles (unit: m/s) for each rainfall propagation group during the experimental period (January-February for 2013, 2016 and 2018) at Townsville airport station (19.25ºS, 146.76 ºE) for (a) sounding data and (b) AUS2200 simulations. The shaded regions indicate one standard deviation. Note that only days showing consistency between observations and model simulations are considered.

The influence of the vertical structure of the zonal wind profile on the rainfall propagation patterns suggests a dependence on large scale climate modes. Figure 15a shows the distribution of various rainfall propagation types in different MJO phases. To increase the sample sizes, all observation days are included in this analysis. Offshore rainfall propagation is observed in all MJO phases except phase 6. However, it is more frequent during phase 4, which is the transition from suppressed to enhanced convection phases of the MJO in northern Australia. In contrast, onshore rainfall propagation tends to occur more frequently during phase 2, a suppressed convection phase of the MJO. The highest occurrence of the no rainfall propagation group is observed during phase 7, an enhanced convection phase of the MJO. To better understand the impact of the MJO on rainfall propagation distribution, the vertical profiles of wind anomalies for these three MJO phases are presented in Fig. 15b. During phase 4 (grey line), low-level easterly anomalies and upper-level westerlies anomalies are evident, which is reminiscent of the vertical wind profile of offshore rainfall propagation (grey line in Fig. 14). This suggests that phase 4 of the MJO provides favorable conditions for offshore rainfall propagation. Similarly, phase 2 (blue line) exhibits easterly anomalies from the surface up to 200 hPa, indicating a strengthening of the easterly trade winds during this phase, which favors onshore rainfall propagation. Phase 7 of the MJO (orange line) shows a weak low-level westerly anomaly (until 900 hPa) and upper-level easterly anomalies (above 800 hPa). These wind characteristics are relatively similar to those of the no rainfall propagation group (e.g., low-level westerly winds and mid-level easterly winds). With the limited sample size from the three MJO

events analyzed in this study, our results suggest that specific rainfall propagation types are more likely to occur during certain MJO phases, and that this may be strongly linked to the MJO-scale modulation of the zonal wind, as well as a possible modifications to the background moisture that is not addressed here. Note that a similar analysis is conducted for days consistent between observations and model simulations. Although the sample size is smaller in each MJO phase, the results are similar (not shown).

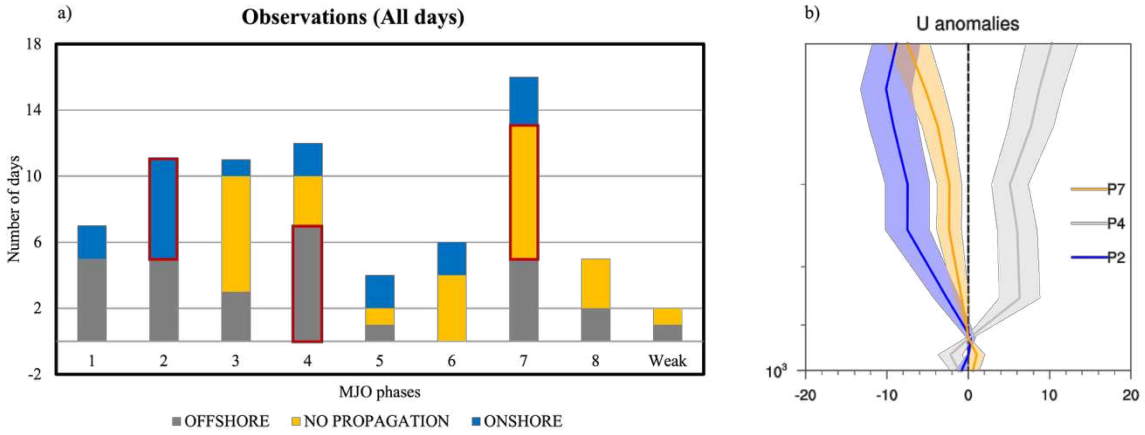

Figure 15: (a) The distribution of rainfall propagation types with MJO phases during the experimental period (January-February for 2013, 2016 and 2018), (b) Vertical profile of zonal wind anomalies (unit: m/s) for three MJO phases. The red outline highlights the MJO phases with the highest number of days for offshore, onshore and no propagation groups. The shaded regions indicate one standard deviation.

4 Discussions and Conclusions

Recent observational studies have demonstrated that the influence of large-scale climate mode variability on coastal rainfall in Northeast Australia is further modulated by local-scale processes (Wu and Leonard, 2019; Dao et al., 2023, 2025). However, the physical mechanisms underlying these scale-interactions are still an open question, partly due to the limited availability of high-resolution simulations capable of capturing a wide range of spatial and temporal scales. This study examines the interaction between mesoscale processes and large-scale forcings in modulating coastal rainfall over the northern Queensland using high-resolution AUS2200 simulations with a horizontal grid spacing of 2.2 km. Our analyses are based on 180 simulation days from three strong MJO events under different ENSO conditions: January/February for 2013 (ENSO neutral), 2016 (El Niño) and 2018 (La Niña).

Spatially inhomogeneous rainfall patterns over coastal regions are evident in both radar observations and model simulations. Our results indicate that rainfall propagation is one of the factors contributing to the inhomogeneous precipitation pattern along the coast by modulating the average rainfall distribution. For example, offshore rainfall propagation generally leads to a widespread rainfall pattern across the entire coastal radar domain, while onshore rainfall propagation results in higher rainfall amounts over the ocean part. In contrast, the no rainfall propagation group is associated with higher average rainfall over the land areas of the radar

domain. This finding is consistent with previous studies in the deep tropics demonstrating that diurnal rainfall propagation influences the distribution and intensity of coastal precipitation (Coppin et al., 2020, Yang and Du, 2022).

Our results show that large-scale background winds and mesoscale land-sea breezes are two important factors controlling rainfall propagation near the coast of northern Queensland. The key findings are summarized in the schematic diagram in Fig. 16. For offshore rainfall propagation, rainfall is typically triggered over land during the afternoon by sea breezes and then propagates offshore during the nighttime with land breezes and large-scale upper-level westerly winds. This is consistent with the previous studies in the deep tropics, which highlight the influence of land breezes (Vincent and Lane 2016, Bai et al., 2021 and Peatman et al., 2023) and large-scale background winds (Short et al., 2019, Natoli and Maloney 2022, 2023) in driving offshore rainfall near the coast. Onshore rainfall propagation tends to occur on days with strong and deep easterly trade winds. Rainfall in this group is associated with the interaction of easterly trade winds and topography, a key synoptic-scale process influencing rainfall along the Queensland coast (Lyons and Bonnell, 1992; Connor and Bonnell, 1998, Klingaman, 2012). For the no propagation group, rainfall is initiated during the afternoon due to the convergence of sea breezes and low-level background westerlies, and it persists over land during the nighttime under the influence of strong easterly winds extending from surface to the mid-levels of the atmosphere.

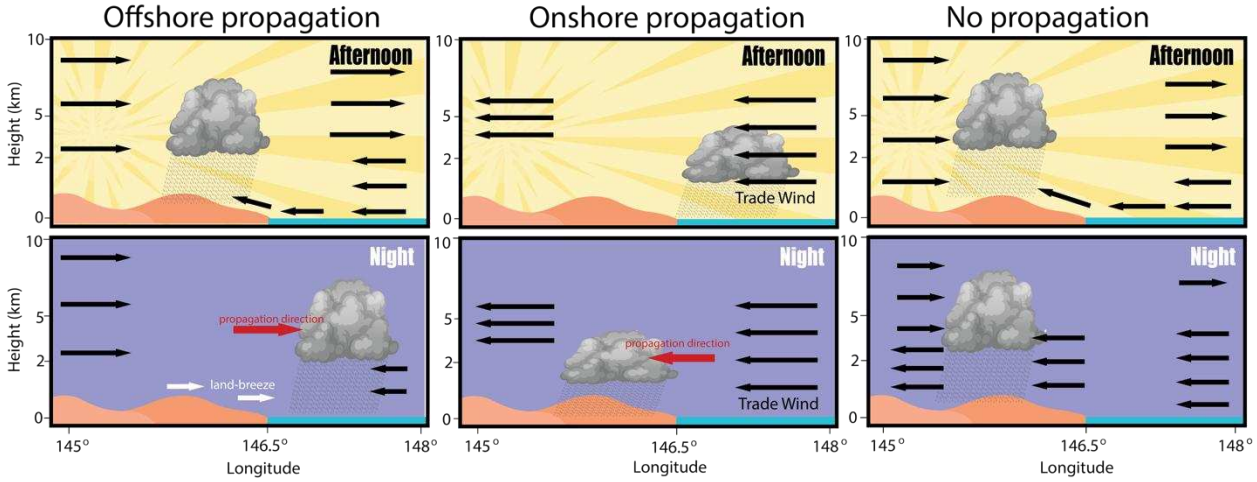

Figure 16: Schematic diagram illustrating the vertical structure of winds for different rainfall propagation groups. Black vectors represent wind direction and amplitude in the afternoon and at night, white vectors indicate land breezes, and red vectors show the rainfall propagation direction. The land (ocean) is shown in orange (blue).

Gravity waves are also known as an important factor controlling offshore rainfall propagation in the deep tropics (Love et al., 2011; Hassim et al., 2016; Yokoi et al., 2017; Coppin and Bellon 2019) and although they may not lead to an organized squall line, their influences are dominant farther offshore (Vincent and Lane 2016, Bai et al., 2021 and Peatman et al., 2023). Offshore propagation speeds in this study (approximately 5 m/s) are consistent with the near-shore part of the offshore propagation found in the deep tropics by Peatman et al. (2014), Vincent and Lane (2016), and much slower than the gravity wave speed (approximately 15 m/s, Love et al., 2011; Peatman et al., 2023). As this study focuses on understanding the

physical mechanisms behind the inhomogeneous rainfall patterns observed along northern Queensland's coastal areas, we primarily focus on processes (e.g., the land-sea breeze and the large-scale background winds) that affect rainfall propagation near the coast. Future research could explore the role of gravity waves in the distribution of rainfall farther offshore.

The onshore rainfall propagation group in this study exhibits several interesting features that require further investigation. For example, a secondary rainfall peak is observed over the ocean during the nighttime (around 22 LT), along with evidence of offshore propagation of nocturnal oceanic rainfall. Bai et al., (2021) found that low-level convergence resulted from the interaction of offshore land breeze and onshore background wind is the key mechanism driving nocturnal offshore rainfall propagation near the west coast of Sumatra. Other factors such as gravity waves (Mapes et al., 2003; Love et al., 2001; Du and Rotunno 2018), the direction and intensity of the background wind (Wang and Sobel 2017; Du and Rotunno 2018), inertial oscillation (Du et al., 2014; Xue et al., 2018) can also affect the nocturnal offshore rainfall propagation. A more detailed quantitative analysis is needed to fully understand these processes, which is beyond the scope of the present study.

This study also discusses the relationship between rainfall propagation and the MJO. We found that specific MJO phases may provide favorable conditions for certain types of rainfall propagation. For example, phase 4 of the MJO (transition phase) has conditions that support offshore rainfall propagation. Natoli and Maloney (2023) also noted that the transition from suppressed phases to enhanced phase of the boreal summer intraseasonal oscillation (BSISO) provides favorable conditions for a strong diurnal cycle and offshore rainfall propagation over Luzon Island. Given the clear dependence on the vertical wind profile demonstrated in this paper, we hypothesize that a key mechanism by which the MJO modifies the offshore propagation in this region is via changes to the background wind. Changes in the strength of the land-sea breeze circulation arising due to feedbacks between clouds, moisture and net radiative heating of the surface may be a secondary influence. However, due to the limited sample size in this study, there are still some uncertainties in the MJO-rainfall propagation relationship. Future studies with larger sample sizes are needed to re-examine the relationship between rainfall propagation and large-scale climate variability.

Scale interaction between atmospheric convection and large-scale dynamics is two-way in the tropics. The diurnal cycle of rainfall in tropical coastal and island regions can also modulate large-scale atmospheric variabilities such as the MJO and ENSO. Over the Maritime Continent, diurnal rainfall propagation can either facilitate or inhibit MJO eastward propagation, depending on its phase alignment with MJO convection (Peatman et al., 2014; Birch et al., 2016; Hagos et al., 2016). Our results indicate that rainfall propagation modulates average rainfall patterns and therefore could potentially influence rainfall anomalies associated with different MJO and ENSO phases. This may help explain the occurrence of localized enhanced rainfall during the suppressed MJO phases or El Niño events, as observed in Dao et al. (2023; 2025. Future studies could look at impact of these different rainfall propagations on larger-scale variability. Further research is also needed to better understand the upscale impacts of mesoscale processes on tropical climate dynamics.

Although high-resolution simulations have been used in previous studies to understand the impact of scale interactions on coastal rainfall over the deep tropics (Birch et al., 2016; Vincent and Lane 2018; Wei et al., 2020), to the best of our knowledge, this is the first study to

examine the impact of the interaction between large-scale and local-scale forcings on modulating coastal rainfall in Queensland using high resolution simulations. This region is unique because of the influence of persistent easterly trade winds at low- and mid-levels, and the influence of the mid- latitude weather systems. These aspects mean that this region has distinct drivers of coastal rainfall that set it aside from locations in the deep tropics. Our findings help better understand the processes that control spatially inhomogeneous coastal rainfall patterns over northern Queensland. This is important for assessing the impact of climate change on rainfall and extreme events at the local coastal scale, which is critical for the numerous coastal communities and cities in the region. Given that Queensland is an important agricultural area, the findings also have potential values for water resource and agricultural management.

Acknowledgments

T. L. Dao was funded by the Melbourne Research Scholarship, the Rowden White Scholarship, the Australian Research Council (ARC) Centre of Excellence for Climate Extremes (CE170100023). C. L. Vincent and Y. Huang were supported by the Australian Research Council (ARC) Centre of Excellence for the Weather of the 21st Century (CE230100012). S. C. Peatman and C. E. Birch were funded by the UK's National Environment Research Council (NERC) through the TerraMaris project, grant NE/R016739/1. Analysis was performed using the National Computing Infrastructure (NCI) National Facility. We thank Paola Petrelli for her help with data processing.

Conflict of interest statement

The authors have no conflicts of interest to declare

Data Availability Statement

The AUS2200 dataset is available at National Computational Infrastructure (NCI) from https://dx.doi.org/10.25914/1cz8-vk42 (ENSO La Niña), https://dx.doi.org/10.25914/yj50-dm80 (ENSO El Niño), and https://dx.doi.org/10.25914/gprx-2d45 (ENSO Neutral). The Australian Unified Radar Archive data level 2 dataset (Soderholm et al., 2022) is available at NCI under a CC4-BY-NC license from https://dx.doi.org/10.25914/JJWZ-0F13. Daily upper-air soundings were downloaded from the University of Wyoming (https://weather.uwyo.edu/upperair/sounding.html). The ERA5 reanalysis data are from Copernicus Climate Change Service Climate Data Store (https://cds.climate.copernicus.eu/cdsapp#!/dataset/reanalysisera5-pressure-levels). IMERG data

753 are provided by the NASA/Goddard Space Flight Center's Precipitation Processing Center. The
754 datasets are archived at the NASA GES DISC (https://disc.gsfc.nasa.gov). The Real-time
755 Multivariate MJO (RMM) index was downloaded from the Australia Bureau of Meteorology
756 (http://www.bom.gov.au/climate/mjo/) The codes can be made available by the corresponding
757 author upon reasonable request.

758 **References**

759 Bai, H., and Coauthors (2021). Formation of nocturnal offshore rainfall near the west coast of
760 Sumatra: Land breeze or gravity wave? *Monthly Weather Review*, *149*, 715–731.
761 https://doi.org/10.1175/MWR-D-20-0179.1.

762 Best, M. J., Pryor, M., Clark, D. B., Rooney, G. G., Essery, R. L. H., Ménard, C. B., Edwards, J.
763 M., Hendry, M. A., Porson, A., Gedney, N., Mercado, L. M., Sitch, S., Blyth, E., Boucher,
764 O., Cox, P. M., Grimmond, C. S. B., and Harding, R. J.: The Joint UK Land Environment
765 Simulator (JULES), model description – Part 1: Energy and water fluxes, Geosci. Model
766 Dev., 4, 677–699, https://doi.org/10.5194/gmd-4-677-2011, 2011.

767 Birch, C. E., D. J. Parker, A.O'Leary, J.H. Marsham, C. M. Taylor, P. P. Harris, and G. M. S.
768 Lister, 2013: Impact of soil moisture and convectively generated waves on the initiation of
769 a West African mesoscale convective system. Quart. J. Roy. Meteor. Soc., 139, 1712–1730,
770 https://doi.org/10.1002/qj.2062.

771 Birch, C. E., Webster, S., Peatman, S. C., Parker, D. J., Matthews, A. J., Li, Y., & Hassim, M. E.
772 E. (2016). Scale Interactions between the MJO and the Western Maritime Continent.
773 *Journal of Climate*, *29*(7), 2471-2492. https://doi.org/10.1175/JCLI-D-15-0557.1

774 Black, M. T., and T. P. Lane, 2015: An improved diagnostic for summertime rainfall along the
775 eastern seaboard of Australia. *Int. J. Climatol.*, **35,** 4480-4492,
776 https://doi.org/10.1002/joc.4300.

777 Brown, A., S. Milton, M. Cullen, B. Golding, J. Mitchell, and A. Shelly (2012), Unified modeling
778 and prediction of weather and climate: A 25-year journey, Bull. Am. Meteorol. Soc., 93,
779 1865–1877.

780 Bui, H. X., Maloney, E. D., Short, E., & Riley Dellaripa, E. M. (2023). Diurnal cycle of wind
781 speed and precipitation over the northern Australia coastal region: CYGNSS
782 observations. *Geophysical Research Letters, 50*, e2023GL103005.

Clark, D. B., Mercado, L. M., Sitch, S., Jones, C. D., Gedney, N., Best, M. J., Pryor, M., Rooney, G. G., Essery, R. L. H., Blyth, E., Boucher, O., Harding, R. J., Huntingford, C., and Cox, P. M.: The Joint UK Land Environment Simulator (JULES), model description – Part 2: Carbon fluxes and vegetation dynamics, Geosci. Model Dev., 4, 701–722, https://doi.org/10.5194/gmd-4-701-2011, 2011

Connor, G. J. and M. Bonnell, 1998: Air mass and dynamic parameters affecting trade wind precipitation on the Northeast Queensland tropical coast. Int. J. Climatol., 18, 1357–1372

Coppin, D., and G. Bellon, 2019: Physical mechanisms controlling the offshore propagation of convection in the tropics: 1. Flat island. J. Adv. Model. Earth Syst., 11, 3042–3056, https://doi.org/10.1029/2019MS001793.

Coppin, D., and G. Bellon, A. Pletzer, and C. Scott, 2020: Detecting and tracking coastal precipitation in the tropics: Methods and insights into multiscale variability of tropical precipitation. J. Climate, 33, 6689–6705, https://doi.org/10.1175/JCLI-D-19-0321.1.

Cowan, T., and Coauthors, 2019: Forecasting the extreme rainfall, low temperatures, and strong winds associated with the northern Queensland floods of February 2019. *Wea. Climate Extremes*, **26,** 100232, https://doi.org/10.1016/j.wace.2019.100232.

Cowan, T., Wheeler, M. C., & Marshall, A. G. (2023). The Combined Influence of the Madden–Julian Oscillation and El Niño–Southern Oscillation on Australian Rainfall. *Journal of Climate*, *36*(2), 313-334. https://doi.org/10.1175/JCLI-D-22-0357.1

Dao, T. L., Vincent, C. L., & Lane, T. P. (2023). Multiscale Influences on Rainfall in Northeast Australia. *Journal of Climate*, *36*(17), 5989-6006. https://doi.org/10.1175/JCLI-D-22-0835.1

Dao, T. L., Vincent, C. L., Huang,Y., Soderholm, J. S. (2025).Modulations of local rainfall in Northeast Australia associated with the Madden Julian Oscillation. *Quarterly Journal of the Royal Meteorological Society* (submitted)

Davies, R. (2024). Tropical Cyclone Jasper, Queensland, Australia - December 2023. *Emergency Management Service*

Dipankar, A., S. Webster, X.-Y. Huang, and V. Q. Doan, 2019: Understanding biases in simulating the diurnal cycle of convection over the western coast of Sumatra: Comparison with pre-YMC observation campaign. Mon. Wea. Rev., 147, 1615– 1631, https://doi.org/10.1175/MWR-D-18-0432.1.

Du, Y., Zhang, Q., Chen, Y.-L., Zhao, Y., & Wang, X. (2014). Numerical simulations of spatial distributions and diurnal variations of low-level jets in China during early summer. Journal of Climate, 27(15), 5747–5767. https://doi.org/10.1175/JCLI-D-13-00571.1

Du, Y., and R. Rotunno, 2018: Diurnal cycle of rainfall and winds near the south coast of China. Journal of the Atmospheric Sciences, 75, 2065–2082, https://doi.org/10.1175/JAS-D-17-0397.1.

Fang, J., Du, Y. A global survey of diurnal offshore propagation of rainfall. *Nat Commun* **13**, 7437 (2022). https://doi.org/10.1038/s41467-022-34842-0

Ghelani, R. P. S., Oliver, E. C. J., Holbrook, N. J., Wheeler, M. C., & Klotzbach, P. J. (2017). Joint Modulation of Intraseasonal Rainfall in Tropical Australia by the Madden-Julian Oscillation and El Niño-Southern Oscillation. *Geophysical Research Letters*, *44*(20), 10,754-710,761. https://doi.org/10.1002/2017GL075452

Gillett, Z. E., Taschetto, A. S., Holgate, C. M., and Santoso, A.: Linking ENSO to synoptic weather systems in eastern Australia, Geophys. Res. Lett., 50, e2023GL104814, https://doi.org/10.1029/2023GL104814, 2023.

Goodwin, I. D. (2022). The Weather behind the Eastern Australian floods-the storm cluster from 23rd February to 2nd April. *Risk frontiers, Briefing Note 464.*

Gregory, C. H., Holbrook, N. J., Spillman,C. M., & Marshall, A. G. (2024).Combined role of the MJO and ENSO inshaping extreme warming patterns andcoral bleaching risk in the Great BarrierReef. Geophysical Research Letters, 51,e2024GL108810. https://doi.org/10.1029/2024GL108810.

Hassim, M. E. E., T. P. Lane, and W. W. Grabowski, 2016: The diurnal cycle of rainfall over New Guinea in convection permitting WRF simulations. Atmos. Chem. Phys., 16, 161–175, https://doi.org/10.5194/acp-16-161-2016.

Huang, Y., Arblaster, J., & Lane, T. (2024). AUS2200: A High-Resolution Regional Atmospheric Modeling Dataset [Data set]. https://doi.org/10.25914/w95d-q328.

Huffman, G. J., E. F. Stocker,D. T. Bolvin, E. J. Nelkin, and J. Tan, 2019: GPM IMERG final precipitation L3 half hourly 0.1 degree 3 0.1 degree V06 (GPM_3IMERGHH). GES DISC, accessed 24 November 2022, https://doi.org/10.5067/ GPM/IMERG/3B-HH/06.

Jones, D. A., W. Wang, and R. Fawcett, 2009: High-quality spatial climate data-sets for Australia. *Aust. Meteorol. Oceanogr. J.*, **58,** 233, https://doi.org/10.22499/2.5804.003

Jones, R.W., Sanchez, C., Lewis, H., Warner, J., Webster, S. and Macholl, J., 2023. Impact of domain size on tropical precipitation within explicit convection simulations. Geophysical Research Letters, 50(17), 466 p.e2023GL104672.

King, A. D., L. V. Alexander, and M. G. Donat, 2013: Asymmetry in the response of eastern Australia extreme rainfall to low-frequency Pacific variability. *Geophys. Res. Lett.*, **40,** 2271–2277, https://doi.org/10.1002/grl.50427.

Klingaman, N.P., 2012: A literature survey of key rainfall drivers in Queensland, Australia: Rainfall variability and change. QCCCE Research Report: Rainfall in Queensland. Part 1. Department of Environmental and Resource Management, Queensland Government, Brisbane, Australia.

Lestari, S., King, A., Vincent, C., Protat, A., Karoly, D., & Mori, S. (2022). Variability of Jakarta Rain-Rate Characteristics Associated with the Madden–Julian Oscillation and Topography. *Monthly Weather Review*, *150*(8), 1953-1975. https://doi.org/10.1175/MWR-D-21-0112.1

Lough, J. M., 1991: Rainfall variations in Queensland, Australia: 1891–1986. *Int. J. Climatol.*, **11,** 745-768, https://doi.org/10.1002/joc.3370110704.

Love, B. S., Matthews, A. J., & Lister, G. M. S. (2011). The diurnal cycle of precipitation over the Maritime Continent in a high-resolution atmospheric model. *Quarterly Journal of the Royal Meteorological Society*, *137*(657), 934-947. https://doi.org/10.1002/qj.809

Lyons, W. F. and M. Bonnell, 1992: Daily meso-scale rainfall in the tropical wet/dry climate of the Townsville area, North-east Queensland

Mapes, B. E., Warner, T. T., Xu, M., & Negri, A. J. (2003a). Diurnal patterns of rainfall in northwestern South America. Part I: Observations and context. Monthly Weather Review, 131(5), 799–812. https://doi.org/10.1175/1520-0493(2003)131<0799:dporin>2.0.co;2

Mapes, B. E., Warner, T. T., & Xu, M. (2003b). Diurnal patterns of rainfall in northwestern South America. Part III: Diurnal gravity waves and nocturnal convection offshore. Monthly Weather Review, 131(5), 830–844. https://doi.org/10.1175/1520-0493(2003)131<0830:dporin>2.0.co;2

873 Marshall, A. G., Hendon, H. H., & Hudson, D. (2021). Influence of the Madden-Julian
874 Oscillation on multiweek prediction of Australian rainfall extremes using the ACCESS-
875 S1 prediction system. *Journal of Southern Hemisphere Earth Systems Science*, *71*(2),
876 159-180. https://doi.org/10.1071/ES21001
877 McBride, J. L., and N. Nicholls, 1983: Seasonal relationships between Australian rainfall and the
878 Southern Oscillation. *Mon. Wea. Rev.,* **111,** 1998-2004, https://doi.org/10.1175/1520-
879 0493(1983)111<1998:SRBARA>2.0.CO;2.
880 Mori, S., and Coauthors, 2004: Diurnal land–sea rainfall peak migration over Sumatera Island,
881 Indonesian Maritime Continent, observed by TRMMsatellite and intensive rawinsonde
882 soundings. Mon. Wea. Rev., 132, 2021–2039, https://doi.org/10.1175/1520
883 0493(2004)132,2021:DLRPMO.2.0.CO;2.
884 Murphy, B. F., and J. Ribbe, 2004: Variability of southeastern Queensland rainfall and climate
885 indices. *Int. J. Climatol.*, **24,** 703-721, https://doi.org/10.1002/joc.1018.
886 Natoli, M. B., & Maloney, E. D. (2022). The tropical diurnal cycle under varying states of the
887 monsoonal background wind. *Journal of the Atmospheric Sciences*.
888 https://doi.org/10.1175/jas-d-22-0045.1
889 Natoli, M. B., & Maloney, E. D. (2023). Environmental controls on the tropical island diurnal
890 cycle in the context of intraseasonal variability. *Journal of Climate*.
891 https://doi.org/10.1175/JCLI-D-22-0824.1
892 Peatman, S. C., Matthews, A. J., & Stevens, D. P. (2014). Propagation of the Madden–Julian
893 Oscillation through the Maritime Continent and scale interaction with the diurnal cycle of
894 precipitation. *Quarterly Journal of the Royal Meteorological Society*, *140*(680), 814-825.
895 https://doi.org/10.1002/qj.2161
896 Peatman SC, Matthews AJ, Stevens DP (2015) Propagation of the Madden–Julian oscillation and
897 scale interaction with the diurnal cycle in a high-resolution GCM. Clim Dyn 45:2901–2918
898 Peatman, S. C., Birch, C. E., Schwendike, J., Marsham, J. H., Dearden, C., Webster, S., Neely,
899 R. R., & Matthews, A. J. (2023). The role of density currents and gravity waves in the
900 offshore propagation of convection over Sumatra. *Monthly Weather Review, 151*, 1757–
901 1777.

902 Pepler, A. S., A. J. Dowdy, P. van Rensch, I. Rudeva, J. L. Catto, and P. Hope, 2020: The
903 contributions of fronts, lows and thunderstorms to southern Australian rainfall. *Climate*
904 *Dyn.,* **55,** 1489-1505, https://doi.org/10.1007/s00382-020-05338-8.
905 Power, S., M. Haylock, R. Colman, and X. Wang, 2006: The predictability of interdecadal changes
906 in ENSO activity and ENSO teleconnections. *J. Climate*, **19,** 4755-4771,
907 https://doi.org/10.1175/JCLI3868.1
908 Rauniyar, S. P., & Walsh, K. J. E. (2016). Spatial and temporal variations in rainfall over Darwin
909 and its vicinity during different large-scale environments. *Climate Dynamics*, *46*(3), 671-
910 691. 10.1007/s00382-015-2606-1
911 Smith, M., M. J. Poggio, M. Thompson, and A. Collier, 2014: The Economics of Pesticide
912 Management Practices on Sugarcane Farms: Final Synthesis Report. Department of
913 Agriculture, Fisheries and Forestry (DAFF), Queensland.
914 Soderholm, J., Louf, V., Brook, J., Protat, A., & Warren, R. (2022). Australian Operational
915 Weather Radar Level 2 Dataset. In *National Computing Infrastructure*.
916 https://doi.org/10.25914/JJWZ-0F13
917 Su, C.-H., et al. (2022). BARRA2: Development of the next-generation Australian regional
918 atmospheric reanalysis. In *Australian Bureau of Meteorology*.
919 Twomey, C. R., and A. S. Kiem, 2021: Australian rainfall variability—Why is the eastern seaboard
920 of Australia different to the rest of Australia and also internally inhomogeneous. *Int. J.*
921 *Climatol.*, **41,** 5051-5071, https://doi.org/10.1002/joc.7116.
922 Vincent, C. L., and T. P. Lane, 2016: Evolution of the diurnal precipitation cycle with the passage
923 of a Madden–Julian oscillation event through the Maritime Continent. Mon. Wea. Rev., 144,
924 1983–2005, https://doi.org/10.1175/MWR-D-15-0326.1.
925 Vincent, C. L., & Lane, T. P. (2017). A 10-Year Austral Summer Climatology of Observed and
926 Modeled Intraseasonal, Mesoscale, and Diurnal Variations over the Maritime Continent.
927 *Journal of Climate*, *30*, 3807-3828. https://doi.org/10.1175/jcli-d-16-0688.1
928 Vincent, C. L. and T. P. Lane, 2018: Mesoscale variation in diabatic heating around Sumatra, and
929 its modulation with the Madden-Julian oscillation, Monthly Weather Review, 146, 2599–
930 2614, https://doi.org/10.1175/MWR-D-17-0392.1.

Wang, G., and H. H. Hendon, 2007: Sensitivity of Australian rainfall to inter–El Niño variations. *J. Climate*, **20,** 4211-4226, https://doi.org/10.1175/JCLI4228.1.

Wang, S., and A. H. Sobel, 2017: Factors controlling rain on small tropical islands: Diurnal cycle, large-scale wind speed, and topography. Journal of the Atmospheric Sciences, 74, 3515–3532, https://doi.org/ 10.1175/JAS-D-16-0344.1.

Wei, Y., Pu, Z., & Zhang, C. (2020). Diurnal Cycle of Precipitation Over the Maritime Continent Under Modulation of MJO: Perspectives From Cloud-Permitting Scale Simulations. *Journal of Geophysical Research: Atmospheres*, *125*(13). https://doi.org/10.1029/2020JD032529

Wheeler, M. C., & Hendon, H. H. (2004). An All-Season Real-Time Multivariate MJO Index: Development of an Index for Monitoring and Prediction. *Monthly Weather Review*, *132*(8), 1917-1932. https://doi.org/10.1175/1520-0493(2004)132<1917:AARMMI>2.0.CO;2

Wheeler, M. C., H. H. Hendon, S. Cleland, H. Meinke, and A. Donald, 2009: Impacts of the Madden–Julian Oscillation on Australian Rainfall and Circulation. *J. Climate*, **22,** 1482-1498, https://doi.org/10.1175/2008JCLI2595.1.

Wu, E., C. L. Vincent, T. P. Lane, 2019: Diurnal Cycle of Surface Winds in the Maritime Continent Observed through Satellite Scatterometry. *Mon. Wea. Rev.,* 2023-2044, https://doi.org/10.1175/MWR-D-18-0433.1.

Wu, P., M. Hara, J.-I. Hamada, M. D. Yamanaka, and F. Kimura, 2009: Why a large amount of rain falls over the sea in the vicinity of western Sumatra Island during nighttime. J. Appl. Meteor. Climatol., 48, 1345–1361, https://doi.org/10.1175/2009JAMC2052.1.

Wu, W., and M. Leonard, 2019: Impact of ENSO on dependence between extreme rainfall and storm surge. *Environ. Res. Lett.,* **14**, 124043, https://doi.org/10.1088/1748-9326/ab59c2.

Xue, M., Luo, X., Zhu, K., Sun, Z., & Fei, J. (2018). The controlling role of boundary layer inertial oscillations in Meiyu frontal precipitation and its diurnal cycles over China. *Journal of Geophysical Research: Atmospheres*, **123**(10), 5090–5115. https://doi.org/10.1029/2018jd028368

Yang, G., & Slingo, J. (2001). The diurnal cycle in the Tropics. Monthly Weather Review, 129(4), 784–801. https://doi. org/10.1175/1520-0493(2001)129<0784:tdcitt>2.0.co;2

961 Yokoi, S., Y. Nakayama, Y. Agata, T. Satomura, K. Kuraji, and J. Matsumoto, 2012: The
962 relationship between observation intervals and errors in radar rainfall estimation over the
963 Indochina Peninsula. Hydrol. Processes, 26, 834–842, https://doi. org/10.1002/hyp.8297.
964
965